

WetCH₄: A Machine Learning-based Upscaling of Methane Fluxes of Northern Wetlands during 2016-2022

Qing Ying^{1,2*}, Benjamin Poulter², Jennifer D. Watts³, Kyle A. Arndt³, Anna-Maria Virkkala³, Lori Bruhwiler⁴, Youmi Oh^{4,5}, Brendan M. Rogers³, Susan M. Natali³, Hilary Sullivan³, Amanda Armstrong², Eric J. Ward², Luke D. Schiferl⁶, Clayton D. Elder^{7,8}, Olli Peltola⁹, Annett Bartsch¹⁰, Ankur R. Desai¹¹, Eugénie Euskirchen¹², Mathias Göckede¹³, Bernhard Lehner¹⁴, Mats B. Nilsson¹⁵, Matthias Peichl¹⁵, Oliver Sonnentag¹⁶, Eeva-Stiina Tuittila¹⁷, Torsten Sachs^{18,19}, Aram Kalhori¹⁸, Masahito Ueyama²⁰, Zhen Zhang^{1,21*}

¹Earth System Science Interdisciplinary Center, University of Maryland, College Park, MD 20740, USA

²Biospheric Sciences Laboratory, NASA Goddard Space Flight Center, Greenbelt, MD 20771, USA

³Woodwell Climate Research Center, Falmouth, MA 02540, USA

⁴NOAA ESRL, 325 Broadway, Boulder, Colorado, USA

⁵Cooperative Institute for Research in Environmental Sciences (CIRES), University of Colorado, Boulder, CO 80305, USA

⁶Lamont-Doherty Earth Observatory, Columbia University, Palisades, NY, USA

⁷Jet Propulsion Laboratory, California Institute of Technology, Pasadena, CA, USA

⁸Ames Research Center, Earth Science Division, Moffett Field, CA, USA

⁹Natural Resources Institute Finland (Luke), Latokartanonkaari 9, Helsinki, 00790, Finland

¹⁰b.geos, Korneuburg, Austria

¹¹Department of Atmospheric and Oceanic Sciences, University of Wisconsin, Madison, WI 53706, USA

¹²Institute of Arctic Biology, University of Alaska, Fairbanks, AK 99775, USA

¹³Max Planck Institute for Biogeochemistry, Jena, Germany

¹⁴Department of Geography, McGill University, Montreal, QC H3A 0B9, Canada

¹⁵Department of Forest Ecology and Management, Swedish University of Agricultural Sciences, Umeå, Sweden

¹⁶Département de géographie, Université de Montréal, Montréal, QC, Canada

¹⁷University of Eastern Finland, School of Forest Sciences, Joensuu, Finland

¹⁸GFZ German Research Centre for Geosciences, Potsdam, Germany

¹⁹Institute of Geocology, Technische Universität Braunschweig, Braunschweig, Germany

²⁰Graduate School of Agriculture, Osaka Metropolitan University, Japan

²¹National Tibetan Plateau Data Center (TPDC), State Key Laboratory of Tibetan Plateau Earth System, Environment and Resource (TPESER), Institute of Tibetan Plateau Research, Chinese Academy of Sciences, Beijing, 100101, China

41 Correspondence to: Qing Ying (qying@umd.edu) and Zhen Zhang (yuisheng@gmail.com)

42 Abstract

43 Wetlands are the largest natural source of methane (CH₄) emissions globally. Northern wetlands
44 (>45° N), accounting for 42% of global wetland area, are increasingly vulnerable to carbon loss,
45 especially as CH₄ emissions may accelerate under intensified high-latitude warming. However,
46 the magnitude and spatial patterns of high-latitude CH₄ emissions remain relatively uncertain.
47 Here we present estimates of daily CH₄ fluxes obtained using a new machine learning-based
48 wetland CH₄ upscaling framework (WetCH₄) that combines the most complete database of eddy
49 covariance (EC) observations available to date with satellite remote sensing informed
50 observations of environmental conditions at 10-km resolution. The most important predictor
51 variables included near-surface soil temperatures (top 40 cm), vegetation spectral reflectance,
52 and soil moisture. Our results, modeled from 138 site-years across 26 sites, had relatively
53 strong predictive skill with a mean R² of 0.51 and 0.70 and a mean absolute error (MAE) of 30
54 nmol m⁻² s⁻¹ and 27 nmol m⁻² s⁻¹ for daily and monthly fluxes, respectively. Based on the model
55 results, we estimated an annual average of 22.8 ± 2.4 Tg CH₄ yr⁻¹ for the northern wetland
56 region (2016-2022) and total budgets ranged from 15.7 - 51.6 Tg CH₄ yr⁻¹, depending on
57 wetland map extents. Although 88% of the estimated CH₄ budget occurred during the May-
58 October period, a considerable amount (2.6 ± 0.3 Tg CH₄) occurred during winter. Regionally,
59 the West Siberian wetlands accounted for a majority (51%) of the interannual variation in
60 domain CH₄ emissions. Overall, our results provide valuable new high spatiotemporal
61 information on the wetland emissions in the high-latitude carbon cycle. However, many key
62 uncertainties remain, including those driven by wetland extent maps and soil moisture products,
63 incomplete spatial and temporal representativeness in the existing CH₄ flux database – e.g.,
64 only 23% of the sites operate outside of summer months and flux towers do not exist or are
65 greatly limited in many wetland regions. These uncertainties will need to be addressed by the
66 science community to remove bottlenecks currently limiting progress in CH₄ detection and
67 monitoring. The dataset can be found at <https://doi.org/10.5281/zenodo.10802153> (Ying et al.,
68 2024).

69 Keywords

70 Northern high latitudes; wetland; methane (CH₄) flux; eddy covariance; remote sensing;
71 machine learning; data-driven upscaling
72

73 1. Introduction

74 Methane (CH₄) is the second most important greenhouse gas after carbon dioxide (CO₂) and
75 has contributed to around 1/3 of anthropogenic warming (IPCC AR6, 2023). Wetlands are the
76 largest natural source of CH₄ emissions. Northern freshwater wetlands (>45° N) account for
77 roughly 40% of global wetland area (ranging 1.3 - 8.7 million km²; Z. Zhang et al., 2021), yet the
78 amount of CH₄ emissions from this region is highly uncertain – currently estimated to be 22 –
79 49.5 Tg CH₄ yr⁻¹ (Aydin et al., 2011; Baray et al., 2021; Heimann, 2011; Kirschke et al., 2013;

Peltola et al., 2019; Saunio et al., 2020; Treat et al., 2018; Watts et al., 2023). The uncertainties in the estimates of wetland CH₄ emissions are primarily attributed to challenges in mapping vegetated wetlands versus open water leading to double counting (Thornton et al., 2016), seasonal wetland dynamics and uncertainties in estimates on flux rates.

Characterized by nutrient, moisture and hydrodynamic conditions, northern freshwater wetlands are classified as wet tundra in treeless permafrost areas, peat-forming bogs and fens in boreal and temperate biomes, and permafrost bogs (Olefeldt et al., 2021; Kuhn et al., 2021). Bogs were estimated to cover the largest area (1.38-2.41 million km²) in the northern high latitudes, followed by fens (0.76-1.14 million km²) and wet tundra (0.31-0.53 million km²) (Olefeldt et al., 2021). Climate change poses significant threats to these wetlands, affecting their extent and the duration of conditions suitable for wetland formation in permafrost zones (Avis et al., 2011). The rates of CH₄ emissions may increase quickly because of intensified warming at the northern high latitudes (Masson-Delmotte et al., 2021; Rawlins et al., 2010; Rößger et al., 2022; Walsh, 2014; Z. Zhang, Poulter, et al., 2023).

Reflecting CH₄ response to warming, northern wetlands may account for a high portion (~78.5%) of the global surface emissions anomaly of CH₄ in 2020 relative to 2019 (6.0 ± 2.3 Tg CH₄ yr⁻¹) (S. Peng et al., 2022; Z. Zhang, Poulter, et al., 2023). This is concerning as the responses of high latitude CH₄ emissions to a warming and possibly wetting climate could produce a positive carbon-climate feedback (McGuire et al., 2009; Natali et al., 2019). However, the ability of models to account for and predict the spatio-temporal variability of high latitude wetland CH₄ emission rates remain very limited (Treat et al., 2024).

Field observations of gas fluxes typically measure CH₄ exchange between the land and atmosphere at sub-meter to ecosystem (100s of m to km) scales (Bansal et al., 2023; Chu et al., 2021). Tower eddy covariance (EC) methods provide near-continuous measurements over ecosystem-scale footprints ($5 - 100 \times 10^3$ m²), the size of which matches fine to medium resolution satellite remote sensing. Typical EC measurement system records include carbon, water and energy fluxes along with environmental conditions at half-hourly intervals. Long-term EC datasets can support the analysis of daily, monthly, seasonal, or interannual patterns and drivers of carbon fluxes (Baldocchi, 2003). Chambers can also measure CH₄ fluxes, though at sub-meter resolution and small spatial coverage area (Kuhn et al., 2021; Bansal et al., 2023). Most chamber studies have a limited temporal sampling period. To avoid footprint disagreement between EC and chamber measurement techniques, we focused on EC-based CH₄ upscaling in this study.

Data-driven upscaling uses empirical models (Bodesheim et al., 2018; Jung et al., 2011), including machine learning (ML) approaches, to compute CH₄ fluxes. It provides independent estimates to those from process-based models and atmospheric inversions (Bergamaschi et al., 2013; Spahni et al., 2011). These approaches have been used to estimate CH₄ fluxes from various ecosystems such as northern wetlands (Peltola et al., 2019; Virkkala et al., 2023; Yuan et al., 2024), global reservoirs (Johnson et al., 2021), and global aquatic ecosystems (Rosentreter et al., 2021).

Two types of methods are generally used for data-driven upscaling. The first uses a look-up table approach and applies emission rates or emission factors via data synthesis to the corresponding land surface areas, or activity data, over the study region. Emission rates from field observations are associated with environmental drivers that have been spatially characterized and are then applied to the land covers with the same environmental drivers. For example, Rosentreter et al. (2021) collected 2,601 CH₄ flux records measured using various methods through a literature review and characterized emission rates over 15 aquatic ecosystem types to upscale global aquatic CH₄ emissions. The study provided estimates of total and per ecosystem emissions but did not produce spatial distributions and was unable to estimate temporal changes. A similar method was applied for the northern permafrost region, where statistical CH₄ flux rates from the Boreal-Arctic Wetland and Lake CH₄ Dataset (BAWLD-CH₄) were analyzed for emission estimation by wetland type (Kuhn et al., 2021; Ramage et al., 2024). This method favors homogeneous ecosystems and static environments, and the results may be biased for large-scale studies where spatial heterogeneity is prevalent.

Another approach uses ML methods to upscale fluxes (Bodesheim et al., 2018; Tramontana et al., 2016; Yuan et al., 2024). ML models are developed with large training datasets. Generally, ML models can learn from high-dimensional data by optimizing many statistical parameters and identifying variables that are closely associated with spatio-temporally varied CH₄ emissions. The efficient computation cost makes it easier to apply the models over large regions at higher spatial resolutions. Among ML methods, decision-tree-based algorithms have been widely used in upscaling for computation efficiency and prediction performance (Beaulieu et al., 2020; Jung et al., 2020; Virkkala et al., 2021; C. Zhang et al., 2020). Specifically, Random Forests (RF) were utilized in regional to global wetland CH₄ upscaling (Davidson et al., 2017; Feron et al., 2024; McNicol et al., 2023; Peltola et al., 2019) for the robustness and prevention of overfitting to noise in the input data. For example, Peltola et al. (2019) used RF and EC measurements to upscale monthly CH₄ fluxes from the northern wetlands at 0.25°- 0.5° spatial resolution over the 2013-2014 period.

ML-based upscaling studies usually incorporate information from remote sensing to inform wetland extent, changes in vegetation and other surface biophysical properties (Davidson et al., 2017; Virkkala et al., 2023; Watts et al., 2014, 2023). For example, recent ML-based large-scale upscaling approaches used MODIS land surface temperature at night (LST), enhanced vegetation index (EVI), vegetation canopy height, and ancillary environmental variables from remote sensing products (McNicol et al., 2023; Ouyang et al., 2023; Peltola et al., 2019) (See Supporting Materials Text 1 and Table S1 for detailed predicting variables used in existing ML-based wetland CH₄ upscaling products). However, soil moisture and soil temperature, two controlling factors of wetland CH₄ fluxes (Knox et al., 2021; Yuan et al., 2022), were missing in previous ML-based regional to global upscaling studies. Soil moisture has been identified as one of the important controlling factors for freshwater wetland CH₄ fluxes (Euskirchen et al., 2024; Voigt et al., 2023). This is the first ML-based study that incorporates remote sensing constraints from Soil Moisture Active Passive (SMAP) microwave-sensed soil moisture and Moderate Resolution Imaging Spectroradiometer Nadir Bidirectional Reflectance Distribution

Function (BRDF) – Adjusted Reflectance (MODIS NBAR) data. Surface reflectance provides information of vegetation properties that affect the production and transport of CH₄ to the atmosphere, and ecosystem wetness (Alonso et al., 2020; Chen et al., 2013; Houborg et al., 2007; Murray-Hudson et al., 2015; Z. Wang et al., 2018; Entekhabi et al., 2010).

The goal of this study is to develop a scalable framework to upscale daily CH₄ fluxes from EC observations to northern latitude wetlands (>45° N) using the ensemble RF ML approach with a suite of reanalysis and remote sensing products representing spatiotemporal environmental conditions. Our specific objectives are to:

1. compile an updated EC-based CH₄ flux dataset that extends the temporal and spatial coverage of the Fluxnet-CH₄ database (Delwiche et al., 2021) for the northern high latitudes;
2. build RF models of CH₄ fluxes at site-level based on *in-situ* measured [physical](#) variables [which allow us to prioritize the selection of gridded variables for upscaling](#), and then [build ensemble RF models](#) at grid-level using gridded reanalysis inputs and constraints from satellite remote sensing; and
3. apply grid-level models to produce a 10-km gridded daily distribution of CH₄ flux product for the northern high latitudes wetlands using bootstrapped models and their derived uncertainties (Table S1).

Deleted: ensemble

2. Materials and methods

2.1 Overview

The scalable framework of upscaling CH₄ fluxes from EC observations for wetlands (referred to as WetCH₄ hereafter), which selects [physical](#) predictors at the site level and constructs upscaling models at a grid level, is illustrated in Fig. 1. *In situ*, reanalysis, and remote-sensing products were compiled as candidate predictors for modeling (Fig. 1, purple boxes; see section 2.2 for details). We first ran a feature selection, which uses ensemble RF models to choose important predictors from an extensive list of *in situ* variables available from the flux tower sites. Gridded versions of selected site variables were taken from Modern-Era Retrospective analysis for Research and Applications (MERRA2) reanalysis (Gelaro et al., 2017) to model with RF at grid level. We then added remote sensing-based products from MODIS NBAR and SMAP soil wetness, as well as topographic data, to strengthen the model and provide finer delineation of environment gradients based on literature and expert knowledge ([Sturtevant et al., 2012](#); [Poulter et al., 2023](#)). The predictive performance of grid-level models with input variables at their native spatial resolution (except for MERRA2 that were interpolated to 10-km resolution) was then evaluated. We also compared model performance with those from two additional ML algorithms: support vector machines (SVM) and artificial neural network (ANN) (Fig. 1 pink boxes). The [RF](#) algorithm [modeled on all gridded input variables gained](#) the highest mean R² and lowest daily median errors in model predictive performance [and](#) was selected for bootstrap modeling and upscaling the 0.098° (~10km along latitudinal length) gridded time series of daily CH₄ fluxes and ensemble uncertainty estimation (Fig. 1 grey boxes).

Deleted: ML

Deleted: with

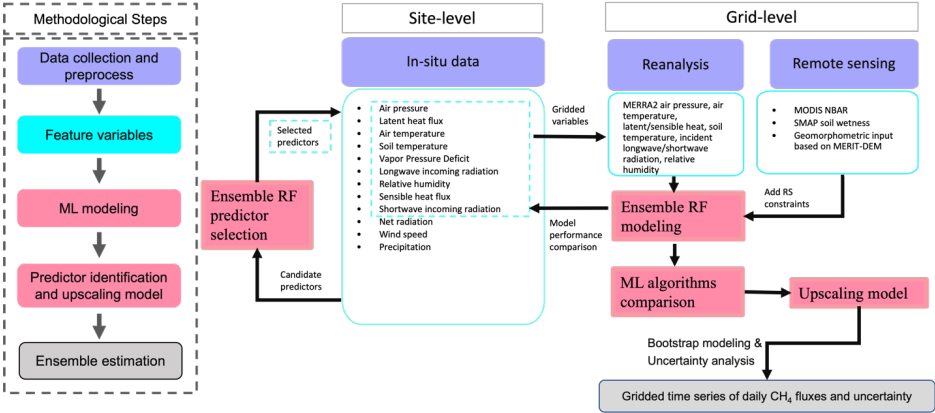


Fig. 1 Workflow and experimental design: abstract methodological steps are integrated in the dashed box on the left, while a detailed experimental design is described on the right. Colors on the right match the associated step on the left.

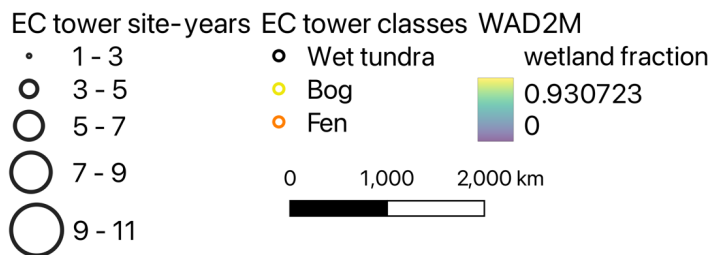
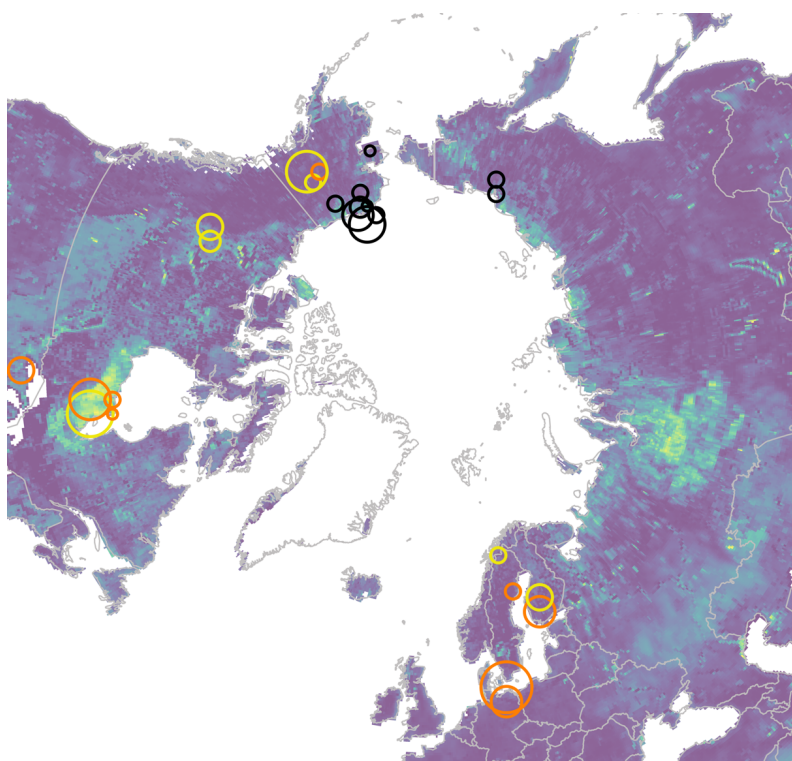


Fig. 2 Eddy covariance tower sites: distribution ($>45^{\circ}$ N), class, and data size (site-years) used in WetCH₄. Colored circles represent EC tower locations and land cover classes, with wetland sites in cyan (wet tundra), yellow (bog) and orange (fen). The circle sizes represent observation years(n) of available CH₄ fluxes at the site (e.g. 1-3 stands for $1 \leq n < 3$). The background image shows the estimated maximum annual fractions of wetland cover in 2011-2020 from WAD2M (Z. Zhang et al., 2021).

2.2 Data

2.2.1 Eddy covariance measurements

The base of our EC data collection stems from a publicly available global synthesis coordination of FLUXNET-CH₄ (Delwiche et al., 2021; Knox et al., 2019), which includes 79 EC tower sites (42 are freshwater wetland sites) and 293 site-years of data. Fluxnet-CH₄ represents a first compilation of global CH₄ fluxes measured by EC towers (Delwiche et al., 2021; Knox et al., 2019), yet more EC data exists outside of the network. We collected both daily and half-hourly data from 44 sites in the northern high latitudes (>45° N), accounting for 167 site years as our base dataset, to which we added data from 6 new sites (31 site-years) and added additional data to 9 existing sites (21 site-years) contributed by principal investigators (Table S2). In total, we assembled data from 50 EC tower sites in northern latitudes (219 site-years), of which 33 are from wetlands (155 site-years), with 13 wet tundra sites, 11 fens, and 9 bogs. Data entries with missing data in gridded predictors were excluded, including 5 wetland sites (FI-LOM, DE-SFN, RU-SAM, RU-VRK, SE-ST1) where data was collected before SMAP data was available. Another 2 sites (CA-BOU, RU-COK) were excluded after quality control revealed an instrument anomaly that affected the measurements. As a result, daily and half-hourly EC data from the 26 wetland sites were compiled for analysis from 22 sites in FLUXNET-CH₄ (among which 8 sites with updated data to recent years including US-ATQ, US-BEO, US-BES, US-BRW, US-IVO, US-NGB, US-NGC, US-UAF) and 4 additional sites using information provided directly by principal investigators (including CA-ARB, CA-ARF, CA-PB1, CA-PB2), consisting of 138 site-years data in total and representing the largest high latitude EC-data compilation for CH₄ to date (Table S2, see Supporting Materials Text 2). The sites were distributed among wetland types, including 9 fens, 7 bogs, and 10 wet tundra sites (Fig. 2). RU-CHE and RU-CH2 were two Chersky sites in East Siberian Russia about 600m apart from each other to form a paired disturbance experiment. RU-CH2 was a control tower over an undisturbed wetland, whereas RU-CHE was a tower affected by artificial drainage. The above-ground conditions of the two sites were virtually identical, but soil temperature and moisture were different. Drainage caused lower CH₄ fluxes at RU-CHE compared to those at RU-CH2. However, the SMAP data could not discern the drainage impact on soil moisture at the RU-CHE site due to a coarser spatial resolution, thus it was excluded from grid-level modeling.

Half-hourly fluxes acquired from FLUXNET-CH₄ were already gap-filled (see Supporting Materials Text 2; Irvin et al., 2021). Additional half-hourly fluxes acquired from site PIs were not gap-filled, and as such we performed per site gap filling following the FLUXNET-CH₄ approach (Irvin et al., 2021; Knox et al., 2019). Gap-filled fluxes were temporally consistent and agreed with validation data (mean $R^2 = 0.68$ and mean RMSE = 6 nmol m⁻² s⁻¹, see Supporting Materials Text 2).

The mean difference in daily mean fluxes between the gap-filled data and the original data converged to -0.2 nmol m⁻² s⁻¹ when there were more than 11 half-hourly EC tower observations in a day but showed substantial bias and larger differences when including days with less than 11 half-hourly observations (Fig. S1). Therefore, daily data entries were only kept when the

Deleted: on the reliable seasonal measurements as described further down...

number of half-hourly EC tower observations per day was greater than 11. All data were retained on four sites where only daily, quality-filtered, data were provided by site PIs (Table S2). As a result, we identified 12,784 daily data entries for upscaling models (Table S2), spanning 2015-2021 with seasonal observation distributions of 44.0% in June-July-August (JJA), 29.0% in March-April-May (MAM), 24.5% in September-October-November (SON), and 2.5% in December-January-February (DJF) (Fig. S2).

Site-level candidate predictors were identified by their known influences on CH₄ fluxes at multi-day to seasonal scales from field control experiments, *in situ* flux synthesis, and process-based modeling (Bloom et al., 2010, 2017; Knox et al., 2021; Olefeldt et al., 2013, 2017). Only in situ measured physical variables were considered candidate predictors at site-level modeling. *In situ* candidate predictors that were gap-filled and available in FLUXNET-CH₄ included daily averages of air temperature, soil temperature, air pressure, vapor pressure deficit, relative humidity, latent heat flux, sensible heat flux, longwave incoming radiation, shortwave incoming radiation, net radiation, wind speed, and daily total precipitation (Fig. 1 site-level model solid blue box). We were unable to include water-table depth (WTD) or soil water content (SWC) in our site-level model as they were not available at many sites. However, we explored ML results that included WTD or SWC for a subset of individual sites (36% of total) where these variables were available (see Supporting Materials Text 2 for more details).

2.2.2 Reanalysis data and satellite data products

Reanalysis data were used as the gridded input to replace selected predictors at the site level for training the grid-level models and upscaling. These data provided long-term continuous estimates of nearly all the candidate predictors of the *in situ* measured variables (Fig. 1). MERRA2 is an atmospheric reanalysis of the modern satellite era produced by NASA's Global Modeling and Assimilation Office (Gelaro et al., 2017). We calculated daily means for air pressure, surface air temperature, latent heat flux, sensible heat flux, downward-incoming shortwave radiation, downward-incoming longwave radiation, and soil temperature at three depths (9.88 cm, 19.52 cm, 38.59 cm) (Jiao et al., 2023), and relative humidity using the hourly average of surface flux diagnostics, land surface diagnostics, and land surface forcings. The original 0.5° x 0.625° resolution data were resampled to 0.5° grids using a bilinear interpolation method in the NASA MERRA2 web service tool available on GES DISC. The MERRA2 data were further bilinearly interpolated from 0.5° to 0.098° grids weighted by the multiple-error-removed improved-terrain digital elevation model (MERIT-DEM) at 90-m resolution that significantly improves elevation estimates in flat terrain over previous DEM products (Yamazaki et al., 2017). Daily time series of the nearest 0.098° grid to each EC location were extracted for grid-level modeling, whereas daily grids were input for the 10-km upscaling products.

To improve the predictive performance of grid-level models, we added remotely sensed biophysical variables, including SMAP soil wetness, MODIS NBAR bands, and topographic data (Fig. 1, Table 1). All remote-sensing products were extracted in daily time steps and their native spatial resolutions at EC tower sites for modeling and aggregated to 0.098° grids over the study domain for upscaling using Google Earth Engine. We filtered out data gaps in SMAP and

311 MODIS NBAR time series extracted at the native spatial resolution during model training and
312 validation. Gaps in MODIS NBAR were negligible when aggregated from 500-m to 0.098° grids.
313 Gaps in winter SMAP data were filled with zero values to represent frozen soils for upscaling.
314
315 The SMAP soil moisture product is generated using passive microwave radiometer-measured
316 brightness temperature merged with estimates from the GEOS Catchment Land Surface and
317 Microwave Radiative Transfer Model in a soil moisture data assimilation system, providing
318 global products of surface and rootzone soil moisture (Reichle et al., 2017). For soil moisture,
319 we employed Level-4 daily soil wetness products (SPL4SMGP.007) from the SMAP mission as
320 proxies for water-table depth in the grid-level model (Reichle et al., 2017). Surface, rootzone,
321 and soil profile wetness are dimensionless variables that indicate relative saturation for top layer
322 soil (0-5 cm), root zone soil (0-100 cm), and total profile soil (0 cm to model bedrock depth),
323 respectively. These three variables are originally 3-hourly data at 9-km resolution and were
324 converted to daily means.
325
326 Static topographic variables were added as additional attributes in the grid-level model. We
327 used topographical slope and indices that represent the water flow from MERIT-DEM based on
328 Geomorpho90m (Amatulli et al., 2020). Two topographic indices were applied: the compound
329 topographic index (cti) is considered a proxy of the long-term soil moisture availability, and the
330 stream power index (spi, <https://gee-community-catalog.org/projects/geomorpho90/>) reflects the
331 erosive power of the flow and the tendency of gravitational forces to move water downstream.
332 We tested the impact of elevation on model performance in explaining inter-site variability of
333 CH₄ upon the current locations of wetland EC sites (see Supporting Materials Text 6).
334 Nevertheless, elevation was not considered an ecologically controlling factor for wetland CH₄
335 fluxes, and hence was excluded from the input variable importance analysis that ranked the
336 importance of predictors to the prediction accuracy in RF models.
337
338 We included MODIS NBAR (MCD43A4v061) products as predictor variables to represent the
339 vegetation productivity in the grid-level model in order to enhance our model predictive
340 performance in vegetated wetlands. The 7 NBAR bands (including red/green/blue, 2 near
341 infrared, and 2 shortwave infrared) are developed daily at 500-m spatial resolution, using 16
342 days of Terra and Aqua data to remove view angle effects, and it is temporally weighted to the
343 ninth day as the best local solar noon reflectance (Schaaf et al., 2002; Z. Wang et al., 2018).
344 We did not explicitly include a vegetation productivity variable, because such information is
345 retained in MODIS NBAR that is used to produce vegetation indices (e.g. EVI) and gross
346 primary production (GPP). Emergent aerenchymous vegetation is another important component
347 in the plant-mediated pathway of CH₄ transport yet was less represented in existing upscaling
348 models (Table S1).

351 [Table 1.](#) Description of input variables for grid-level upscaling model
352

Variable type	Name	Description	Unit	Data source	Native/Model Spatial resolution	Native Temporal
---------------	------	-------------	------	-------------	---------------------------------	-----------------

Deleted: layer

						resolution
Reanalysis	tas	surface air temperature	°C	MERRA2	0.625°×0.5°/10km	1 hourly
Reanalysis	pa	surface air pressure	Kpa	MERRA2	0.625°×0.5°/10km	1 hourly
Reanalysis	le	latent heat	W m ⁻²	MERRA2	0.625°×0.5°/10km	1 hourly
Reanalysis	h	sensible heat	W m ⁻²	MERRA2	0.625°×0.5°/10km	1 hourly
Reanalysis	rsdl	downward-incoming longwave radiation	W m ⁻²	MERRA2	0.625°×0.5°/10km	1 hourly
Reanalysis	rsds	downward-incoming shortwave radiation	W m ⁻²	MERRA2	0.625°×0.5°/10km	1 hourly
Reanalysis	spfh	surface specific humidity	unitless	MERRA2	0.625°×0.5°/10km	1 hourly
Reanalysis	ts1	soil temperature	° C	MERRA2	0.625°×0.5°/10km	1 hourly
Reanalysis	ts2	soil temperature	° C	MERRA2	0.625°×0.5°/10km	1 hourly
Reanalysis	ts3	soil temperature	° C	MERRA2	0.625°×0.5°/10km	1 hourly
Remote Sensing	sm_s_wetness	surface soil wetness	unitless	SPL4SMGP.007	9 km	3 hourly
Remote Sensing	sm_r_wetness	rootzone soil wetness	unitless	SPL4SMGP.007	9 km	3 hourly
Remote Sensing	sm_p_wetness	profile soil wetness	unitless	SPL4SMGP.007	9 km	3 hourly
Remote Sensing	nbar1	red band	unitless	MCD43A4v061	500 m	daily
Remote Sensing	nbar2	near infrared 1 band	unitless	MCD43A4v061	500 m	daily
Remote Sensing	nbar3	blue	unitless	MCD43A4v061	500 m	daily
Remote Sensing	nbar4	green	unitless	MCD43A4v061	500 m	daily
Remote Sensing	nbar5	near infrared 2 band	unitless	MCD43A4v061	500 m	daily
Remote Sensing	nbar6	shortwave infrared 1 band	unitless	MCD43A4v061	500m	daily
Remote Sensing	nbar7	shortwave infrared 2 band	unitless	MCD43A4v061	500 m	daily
Remote Sensing	slope	terrain slope	radian	Geomorpho90m	90 m	static
Remote Sensing	spi	stream power index	unitless	Geomorpho90m	90 m	static
Remote Sensing	cti	compound topographic index	unitless	Geomorpho90m	90 m	static

355 2.3 Machine learning model

356 2.3.1 General model design

357 We used an RF regression algorithm to train site-level and grid-level ML models (Kim et al.,
358 2020). RF regression builds an assembly of independent trees, each of which is trained from a
359 random subset of input data and tested against the rest of the data (Breiman, 2001). A tree
360 grows two leaves when a random selection of subset features reduces the mean squared error
361 (MSE) of predictions after splitting at a leaf node. Each tree is trained on a bootstrap sample of
362 input data. Trees constructed in this way are less correlated in the ensemble. The generalization
363 error converges as the forest grows to a limit to avoid overfitting. Compared to other ML
364 algorithms, RF has shown to have better accuracy and lower uncertainty (Irvin et al., 2021; Kim
365 et al., 2020). This approach has been previously applied to upscaling CH₄ fluxes in wetlands
366 and rice paddies across multiple ecosystems(Davidson et al., 2017; Feron et al., 2024; McNicol
367 et al., 2023; Ouyang et al., 2023; Peltola et al., 2019).

368
369 A grid-search hyperparameter tuning for daily models was performed before predictor selection.
370 We carried out analyses in Python version 3.6 with the ensemble RF regressor in package
371 'scikit-learn' (Pedregosa et al., 2011). With all the predictors and data, hyper-parameters were
372 set after tuning for optimized model performance, including the number of trees
373 (n_estimators=100), number of variables to consider when looking for the best split
374 (max_features="sqrt", meaning the square root of the total number of feature variables), the
375 maximum depth of the tree (max_depth=10), the minimum number of samples required to split a
376 node (min_sample_split=10), and the minimum number of samples at a leaf node
377 (min_samples_leaf=4).

378
379 For predictor selection and comparisons between the site-level model using *in situ* variables and
380 the grid-level model using gridded versions of *in situ* variables, we built the model across all
381 sites and adopted 5-fold cross-validation and 'out-of-bag' scores from ensemble trees to
382 evaluate model performance, because, at this stage, we aimed to find physically reasonable
383 variables from *in situ* measurements and to compare how the differences in scales and
384 measuring methods between *in situ* predictors and gridded proxies affect model learned
385 temporal variability in CH₄ fluxes. A subset of data was bagged to train each tree in the RF
386 model, with the rest out-of-bag data used as independent validation data to evaluate the
387 prediction accuracy of each tree, resulting in the average out-of-bag scores of all the trees in the
388 model. Cross-validation was applied to daily predictions to select variables that can best predict
389 the daily variability of CH₄ fluxes within sites. The changes in model performance after predictor
390 selection and after switching from site-level variables (*in situ* measurements) to grid-level
391 proxies (reanalysis data) were assessed, which helped quantify differences in model
392 performance when modeling on *in-situ* measured predictor variables versus modeling on
393 substitute variables at grid level. Because the data sources to model input from in situ versus
394 from gridded variables were different, we separated site-level and grid-level modeling to ensure
395 the importance of input features were comparable within a model. The feature importance
396 reflects the relative importance of each input variable in a RF model. It also pertains to the input

Deleted: -

Deleted: -

Deleted: -

Deleted: -

Deleted: -

data distribution and model structure. Therefore, the feature importance by site models can help us identify controlling physical variables, but would not necessarily translate to the same rank in the feature importance of grid models, especially when additional gridded variables from remote sensing products were added to complement the missing controllers from site models.

A summary of input variables for grid-level modeling is provided in Table 1. Although RF can enhance model robustness when collinearity presents in input variables, the collinearity could affect the interpretation of feature importance measured by impurity decrease in RF models. Therefore, we first built a baseline grid-level model with independent variables after a pairwise Pearson correlation test (Fig. S14) to exclude covariates. We grouped significantly correlated variables ($p < 0.001$, $r > 0.8$, white grids except for those on the diagonal line in Fig. S14), forming three groups: SMAP soil moisture variables in group 1 (we also included surface soil moisture that was significantly correlated with the other two soil moisture variables and $r > 0.7$); air temperature (tas), downward longwave radiation (rsdl), spfh, soil temperatures (ts1, ts2, and ts3) in group 2; downward shortwave radiation (rsds) and latent heat (le) in group 3. We then selected one most important variable in each group for the baseline models according to the feature importance of modeling on all predictor variables (Fig. S15). The rest variables out of the groups were included in the baseline features. The resulting baseline features included air pressure (pa), latent heat flux (le), sensible heat flux (h), soil temperature (ts2), rootzone soil wetness (sm_r_wetness), slope, spi, and cti. Then we designed four additional different model settings by changing predictor variables, including (1) baseline variables plus covariates, (2) only variables from MODIS NBAR, (3) baseline variables plus NBAR bands, and (4) all predictor variables. In this forward feature selection process, we evaluated the impacts of adding constraint variables from remote sensing products on model performance.

Model predictive performance evaluates the accuracy of a model to predict at a new site without any prior knowledge. For the spatial predictive performance evaluation of grid-level ML models, we used a nested leave-one-site-out cross-validation scheme (LOOCV, hereafter). Such a scheme selects one site to use as independent validation data to evaluate models trained and tested with data from the remaining sites, repeating the process for all sites. Without any prior knowledge of the validation site added to a model, the LOOCV scheme can assess the predictive ability of the model in a new place as well as evaluate the uniqueness of a site in the dataset. Similar forms of spatial LOOCV have been used to evaluate upscaling models for global or regional CO₂ and CH₄ (McNicol et al., 2023; Peltola et al., 2019; Virkkala et al., 2021). The validation of the upscaling model was not only performed with respect to daily predictions, but also on monthly means. The predictive performance of the upscaling model on monthly variability of CH₄ fluxes and spatial variability across sites is important for studies that vary in temporal and spatial scales.

Model predictive performance was assessed using three evaluation metrics: mean absolute error (MAE), root mean squared error (RMSE), and R² score. Daily modeled CH₄ fluxes were compared to EC observations at each validation site. The evaluation metrics were calculated at daily and monthly scales for each site separately to examine the model performance by general wetland types and for all sites pooled together to evaluate the overall performance and compare

with existing studies. Squared error metrics are more sensitive to outliers and highly skewed data, which is often the case with CH₄ fluxes. Therefore, we selected both MAE and RMSE to quantify the errors. The mean error (ME) between model predictions and validation data was calculated, representing systematic bias in predicted fluxes. The standard deviation of model residuals was also included to measure the spread of the residuals. This matches RMSE when ME equals zero.

Two additional ML algorithms were compared with RF: SVM and ANN. SVM is efficient with sparse data where the dimension of the input space is greater than the number of training samples (Kuter, 2021). While the training process of ANN is expensive and time-consuming, it can develop deep networks with growing training data which may increase predictive performance (Saikia et al., 2020). We used support vector regression to model CH₄ fluxes with the same predictor variables and dataset as used in ensemble RF regressions. Multilayer perceptron regressor is an implementation of an ANN model that adjusts the weights of neurons using backpropagation to improve prediction accuracy. It uses the square error as the loss function and a stochastic gradient-based optimizer 'adam' for weight optimization. We used two hidden layers in the ANN model, each with 50 neurons. Data from all variables were normalized to achieve the best model performance of SVM and ANN.

2.3.2 CH₄ flux upscaling

We trained 500 ensemble RF models with [all gridded](#) predictors of grid-level models from the general model design and with data from all sites for upscaling daily CH₄ fluxes. Each RF model was trained with the same optimized hyper-parameters and different bootstrap samples. Ensemble models were then applied to 0.098° gridded predictors to produce the upscaling CH₄ flux intensities from the means of the 500 predictions and the prediction uncertainty from the standard deviations. Given that the CH₄ fluxes were modeled with data from the wetland EC sites, a wetland extent map was also needed to constrain the areas when scaling grid emissions (see section 2.4). Final CH₄ emission and uncertainty maps associated with wetland extents were the results of multiplying the predicted means and standard deviations of flux intensities with wetland areas. All wetland maps were resampled to 0.098° x 0.098° resolution with a conservative remapping method for producing the emission products.

2.4 Wetland extent maps and benchmark estimates of wetland CH₄ emissions

Wetland extent maps were applied to scale the modeled CH₄ flux intensities to the region. The Wetland Area and Dynamics for CH₄ Modeling (WAD2Mv2), representing spatiotemporal patterns of inundated vegetated wetlands at 0.25° resolution, was selected as the reference for dynamic wetland areas in this study (Z. Zhang et al., 2021). Active and passive microwave detected inundation combined with static wetlands were used to delineate the monthly dynamics of wetland inundation between 2000 and 2020. Open water bodies such as lakes, rivers, reservoirs, coastal wetlands, and rice paddies were excluded. We used monthly mean WAD2M fractions between 2010 and 2020 to represent seasonal wetland dynamics. Emission

estimations are subject to differences in the wetland extent between maps (Saunois et al., 2020). We used monthly means of the Global Inundation Extent from Multi-Satellites (GIEMS2) product (Prigent et al., 2020) to represent temporal patterns of the restricted wetland extents at 0.25° resolution. The coarse resolution maps were resampled to 0.098° x 0.098° grids using the nearest neighbor method. The static Global Lakes and Wetlands Database version 1 (GLWDv1) Level 3 1-km resolution map excluding classes of lakes, rivers, and reservoirs (Lehner & Döll, 2004) was included to quantify the upper limit of wetland cover. For all explicit GLWDv1 wetland classes, we assumed a 100% wetland coverage in the original pixels, except for 'intermittent wetland/lake' for which we assumed a 50% coverage; for GLWDv1 classes represented as extent ranges, we used the average value of the range (i.e., 75% for 50-100% wetland, 37% for 25-50% wetland, and 12% for 0-25% wetland). To support domain emission comparisons, wetland cover was also extracted from the updated GLWD version 2 dataset (GLWDv2, [Lehner et al., 2024](#)) which provides the spatial extent of 33 waterbody and wetland classes at 500-m spatial resolution. All freshwater wetland classes that occur in our study area (classes 8-25) from GLWDv2 were included (i.e., excluding rivers, lakes, reservoirs and other permanent open water bodies, as well as coastal saline/brackish wetlands). The original wetland areas per GLWDv2 pixel were summed across all included classes to derive a total wetland area per pixel. Furthermore, a regional freshwater wetland distribution dataset was calculated from a permafrost region specific land cover map (CALU - circum-Arctic landcover units) which classified 23 land covers including 3 wetland classes and 10 moist to wet tundra classes at 10-m resolution and aggregated to 1km with the majority class (Bartsch et al., 2024). This regional wetland map was applied for CH₄ emission estimation in the North Slope region in Alaska to assess the impacts of different wetland maps on emission estimates in this area when compared against airborne measurements. Wetland areas from the finer resolution maps were aggregated to 0.098° x 0.098° grids for emission calculations.

We compared WetCH₄ emissions with benchmark domain or regional estimates from bottom-up process models, top-down atmospheric observation-based inversions, and existing upscaling studies. We acquired data for the study domain from the ensemble mean of bottom-up process-based models from the Global Carbon Project (GCP) (Z. Zhang, Bansal, et al., 2023) and the extended ensemble of wetland CH₄ estimates that were priors for the top-down GEOS-Chem atmospheric chemical and transport model (WetCHARTs) (Bloom et al., 2017; Friedlingstein et al., 2022). We also included the atmospheric inversions of northern high latitudes from an assimilation CarbonTracker-CH₄ system (Bruhwiler et al., 2014; [update at https://gml.noaa.gov/ccgg/carbontracker-ch4/carbontracker-ch4-2023/](https://gml.noaa.gov/ccgg/carbontracker-ch4/carbontracker-ch4-2023/)). We compared WetCH₄ with existing upscaled products of monthly CH₄ wetland fluxes based on Peltola et al. (2019) for the study domain. For regional wetland hotspots, CH₄ flux estimates were obtained from Carbon in Arctic Reservoirs Vulnerability Experiment (CARVE), which measured total atmospheric columns of CO₂, CH₄, and carbon monoxide over North Alaska in spring, summer, and early fall between 2012 and 2014 (R. Y.-W. Chang et al., 2014; Miller et al., 2016). These were used to verify our seasonal emission estimates over the North Slope region (Zona et al., 2016).

527 3. Results

528 3.1 Model validation

529 3.1.1 Site-level modeling

530 Site-level modeling used all wetland sites to build a RF model and identified the 10 most
531 important variables measured *in situ* that, if left out, decreased the valuation score of the model
532 by more than 90% based on the mean decrease in impurity (Fig. S3). With bootstrap sampling
533 and using all candidate predictors (Fig. 1) in the model, the out-of-bag RMSE of the site-level
534 model was 30.22 nmol m⁻² s⁻¹, and the out-of-bag R² between observed daily means of CH₄
535 fluxes and prediction was 0.73. Modeling with the 10 most important variables at site level
536 resulted in similar model performance, with an out-of-bag RMSE of 30.43 nmol m⁻² s⁻¹ and an
537 out-of-bag R² of 0.73. Site-level model performance converged as the increment of predictor
538 variables ordered by the importance rank (Fig. S4). We then tested building separate models
539 according to wetland types because distinct CH₄ fluxes have been observed from wet tundra
540 (Fig. S5, mean ± standard deviation: 13 ± 14 nmol m⁻² s⁻¹), bogs (22 ± 26 nmol m⁻² s⁻¹) and fens
541 (56 ± 88 nmol m⁻² s⁻¹). The out-of-bag R² (RMSE) was 0.85 (7.2 nmol m⁻² s⁻¹) for bog, 0.84 (27.7
542 nmol m⁻² s⁻¹) for fen, and 0.57 (34.3 nmol m⁻² s⁻¹) for wet tundra. Modeling with the selected 10
543 predictors resulted in an out-of-bag R² (RMSE) of 0.84 (7.6 nmol m⁻² s⁻¹) for bog, 0.84 (27.9
544 nmol m⁻² s⁻¹) for fen, and for 0.53 (36.3 nmol m⁻² s⁻¹) wet tundra. Next, we tested whether the
545 inclusion of non-wetland sites (upland and rice sites) would affect model performance. This
546 resulted in an out-of-bag R² decrease to 0.56 and RMSE increase to 38.86 nmol m⁻² s⁻¹, which
547 suggests that a generalized ML model over all land cover classes is not practical to reliably
548 predict CH₄ fluxes with the current set of predictors and available data. This is most likely due to
549 the distinctive features of CH₄ emissions between wetlands and non-wetland classes (Fig. S5).

Deleted: 4

Deleted: 4

550 3.1.2 Grid-level modeling and remote sensing constraints

551 Substituting *in-situ* measurements of selected predictor variables with gridded MERRA2
552 variables slightly reduced model accuracy. The out-of-bag R² decreased by 9.6% to 0.65 and
553 RMSE increased by 15% to 34.9 nmol m⁻² s⁻¹ compared to the site-level model. The coarse
554 resolution MERRA2 reanalysis data captures less spatial variability of the selected physical
555 variables and is less accurate at the grid-level compared to *in situ* EC measurements.

557 Adding remote sensing constraints to the gridded variables can improve model predictive
558 performance and reduce errors. Modeling on baseline features explained on average 46% of
559 daily CH₄ fluxes' variability in validation sites with the largest range of errors (Fig. 3a). The
560 medians in the baseline model of R², MAE, RMSE, ME under the LOOCV scheme were 0.5,
561 16.4 nmol m⁻² s⁻¹, 21.0 nmol m⁻² s⁻¹ and 6.4 nmol m⁻² s⁻¹, respectively. Adding NBAR or
562 covariates from MERRA2 and SMAP input variables returned a higher mean R² or slightly lower
563 mean errors than the baseline model, whereas modeling with all gridded input variables (the 'all'

model setting) achieved the highest mean R^2 of 0.51 with the comparable mean MAE (23.6 $\text{nmol m}^{-2} \text{s}^{-1}$), RMSE (32.1 $\text{nmol m}^{-2} \text{s}^{-1}$) and ME (0.9 $\text{nmol m}^{-2} \text{s}^{-1}$) (Table S4). Although modeling with baseline features and covariates (the 'base+CoVar' setting) received a comparable mean R^2 with modeling 'all' variables, the latter had a higher median R^2 (0.53) and lower median errors (MAE=14.1 $\text{nmol m}^{-2} \text{s}^{-1}$, RMSE=19.8 $\text{nmol m}^{-2} \text{s}^{-1}$, ME=4.0 $\text{nmol m}^{-2} \text{s}^{-1}$). Our results suggest that including remote sensing constraints or covariates improved models' ability to predict spatial variability in wetland CH_4 fluxes and reduced prediction errors. These results confirm our selection of predictor variables for the upscaling model (Table 1).

The average importance of the baseline features shows their influence on the grid-level model predictive performance (Fig. 3b). Importance of independent predictors under LOOCV scheme, though slightly varied between models, agreed in selecting MERRA2 soil temperature (ts2) as the primary driver in predicting daily CH_4 fluxes in northern wetlands, followed by SMAP rootzone wetness (sm_r_wetness). The eight baseline features accounted for a 99% reduction in the mean validation score of the baseline models. The average importance of 'all' gridded variables used for upscaling (Fig. S15) was consistent with baseline models, emphasizing the importance of soil temperatures and rootzone wetness. Additionally, air pressure and topography also contributed to explaining the daily variability in CH_4 fluxes. Nevertheless, all variables contributed to predicting variability in CH_4 fluxes, showing the complexity of environmental factors that would affect the rates of CH_4 production and the process of gas exchange.

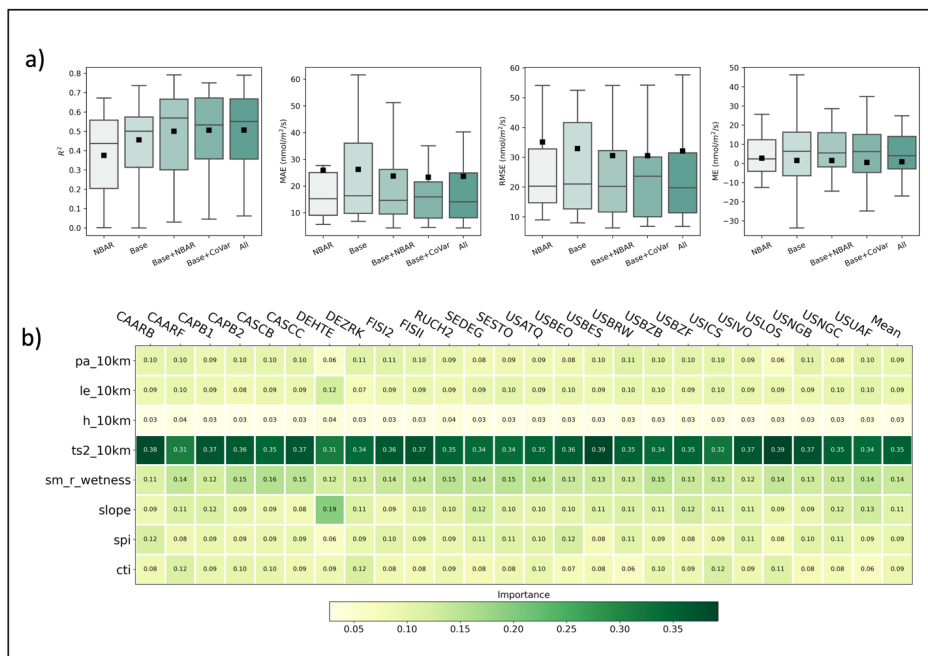


Fig. 3 Grid-level modeling: a) Distribution of R^2 , MAE, RMSE, and ME for all sites (size = 25) in a LOOCV scheme based on gridded data using five model settings: RF modeled using only MODIS NBAR bands, baseline features (MERRA2 air pressure, latent heat flux, sensible heat flux, soil temperature, SMAP rootzone soil wetness, topographic slope, spi, and cit), baseline features plus MODIS NBAR bands, baseline features plus correlated variables within the MERRA2 and SMAP dataset, and all gridded input variables together. The model settings are ranked by mean R^2 , from lowest (left) to highest (right); b) Mean variable importance of baseline models (last column) in the LOOCV scheme and at each site (columns labeled with validation site ID). The values in each column are the means of accumulation of the impurity decrease when a variable was taken out in the trees of a RF model, representing the importance of such variable to the model. The variable names and descriptions refer to Table 1.

Daily mean CH₄ fluxes exhibited great variability in wetlands across space and time (mean = 35 nmol m⁻² s⁻¹, σ = 65 nmol m⁻² s⁻¹, Fig. S3). The model predictive performance (Fig. 4) was calculated for each site and the average performance on the daily variability in CH₄ fluxes was best at wet tundra sites with a mean R^2 of 0.56, followed by bog sites (0.51) and fen sites (0.45). Due to the large variability in fen daily fluxes, errors of daily predictions were highest in fen sites (mean RMSE = 54.2 nmol m⁻² s⁻¹ and mean MAE = 37.8 nmol m⁻² s⁻¹), followed by bog sites (mean RMSE = 27.6 nmol m⁻² s⁻¹ and mean MAE = 22.5 nmol m⁻² s⁻¹), and were lowest in wet tundra sites (mean RMSE = 13.5 nmol m⁻² s⁻¹ and mean MAE = 10.3 nmol m⁻² s⁻¹). Our model slightly overestimated daily fluxes (mean ME = 0.9 nmol m⁻² s⁻¹) was driven by underestimation

of fen sites (mean ME = -12 nmol m⁻² s⁻¹) versus overestimation of bog (mean ME = 14 nmol m⁻² s⁻¹) and wet tundra (mean ME = 3 nmol m⁻² s⁻¹) sites.

Model predictive performance on aggregated monthly means of CH₄ fluxes increased by 37% as compared to daily means (mean R² = 0.70, Fig.4, Table S4). This improvement may be attributed to a better representation of the environmental conditions' average state over a month by the input variables compared to the daily variability. Performance was higher in wet tundra (mean R² = 0.73) and bogs (mean R² = 0.73) and lower in fen sites (mean R² = 0.64, Fig. 4). Mean errors in monthly mean predictions were: RMSE = 28.1 nmol m⁻² s⁻¹, MAE = 21.4 nmol m⁻² s⁻¹, and ME = 0.37 nmol m⁻² s⁻¹ (Table S4). Prediction residuals of daily and monthly CH₄ fluxes (Fig. S6) showed normal distributions for wet tundra sites, indicating the spread of residuals were random errors that increased with the flux magnitude. The residuals had a skewed normal distribution for bog sites indicating likely overestimation. The long-left tails in prediction residuals indicated that the intense emission fluxes from fens during summer peaks were underestimated (Fig. S6).

Site-by-site validation of daily flux predictions varied greatly between individual sites (Fig. 5, S7). For example, US-UAF, an EC site in Interior Alaska with mature black spruce cover and full understory vegetation and mosses over permafrost (Ueyama, Iwata, et al., 2023), which is the only one of the five forest bog sites in our dataset that had low CH₄ fluxes and weak seasonal cycles (less than 10 nmol m⁻² s⁻¹), was significantly overestimated by our model (RMSE = 58 nmol m⁻² s⁻¹ and MAE = 53 nmol m⁻² s⁻¹). Permafrost presence and ground water below soil surface may explain the low fluxes at this site (Iwata et al., 2015; Ueyama, Knox, et al., 2023).

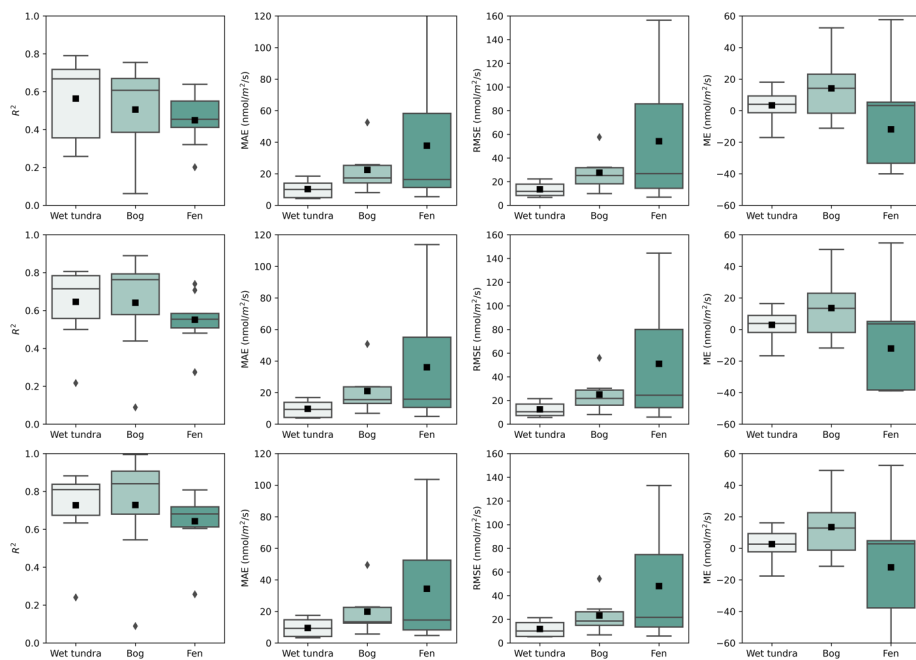


Fig. 4 Model predictive performance evaluation on RF modeled CH₄ fluxes at grid level under LOOCV scheme: boxplots of R^2 , MAE, RMSE, and ME across validation sites by wetland types with mean values denoted in black squares at daily/weekly/monthly (top/middle/bottom panel) time steps.

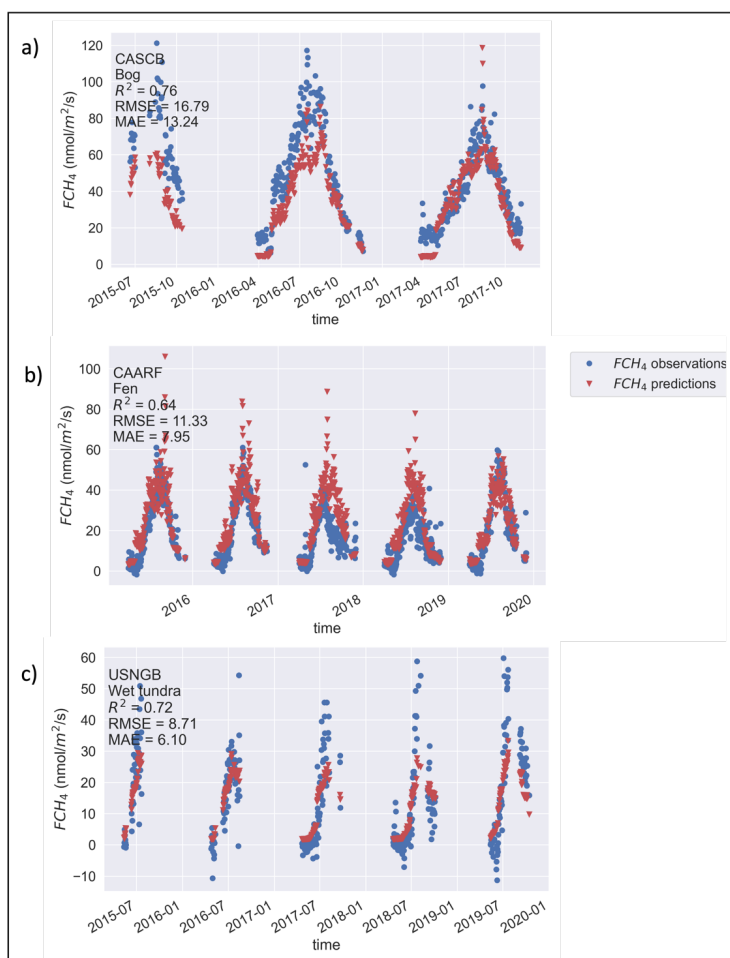


Fig. 5 Example model predictive performance in seasonal cycles of daily FCH₄ at the validation sites of CA-SCB, CA-ARF, and US-NGB, representing bog, fen, and wet tundra, respectively.

3.2 Upscaled wetland CH₄ emissions

3.2.1 Wetland area weighted CH₄ emissions

Upscaled daily CH₄ fluxes were weighted by wetland fraction to estimate gridded daily CH₄ fluxes from northern wetlands based on WAD2Mv2, GIEMS2, and GLWDv1 between 2016 and

2022 (Fig. 6), and GLWDv2 for comparison. The mean annual emissions and RF model associated uncertainties are summarized with different wetland maps in Table S3. The estimate from WetCH₄ with WAD2Mv2 was 22.8 ±2.4 Tg CH₄ yr⁻¹, comparable to UpCH₄ (23.5 ±5.8 Tg CH₄ yr⁻¹). With GIEMS2, WetCH₄ estimated the minimum annual emission of 15.7 ±1.8 Tg CH₄ yr⁻¹. With GLWDv1 and GLWDv2, WetCH₄ estimated potential annual emissions of 46.0 ±5.1 Tg CH₄ yr⁻¹ and 51.6 ±2.2 Tg CH₄ yr⁻¹ for 2016-2022, respectively. The spatial patterns were similar to the post 2016 mean annual fluxes from the GCP process-model ensemble means (28.6 ±21.6 Tg CH₄ yr⁻¹ for 2016-2020), WetCHARTs (29.5 ±30.0 Tg CH₄ yr⁻¹ for 2016-2019), and atmospheric inversions of CarbonTracker-CH₄ (40.9 Tg CH₄ yr⁻¹ for 2016-2022), highlighting the high emission areas in the Hudson Bay Lowlands and West Siberian Lowlands. The emissions from WetCH₄-GIEMS2 were lower in these two hotspots than other estimates. Differences in the distribution of CH₄ emissions between wetland products reflect the influence of wetland dynamics. Mean monthly wetland inundations are provided by WAD2Mv2 and GIEMS2, which set the dynamic limits for the wetland boundaries of the CH₄-emitting surface. While emissions resulting from inundation were captured, it appeared that saturated or wet subsoil conditions were not well represented by WAD2M and GIEMS2, resulting in low emissions in wet yet non-inundated tundra (i.e., Alaska North Slope). To address this, we incorporated wetland fractions from the CALU high-resolution wetland map (Bartsch et al., 2024) specifically produced for the permafrost region in order to estimate Alaska North Slope emissions. Wetland fractions from GLWD (both v1 and v2) represent a static maximum wetland distribution throughout time. Thus, estimates from GLWD may represent the upper bounds for all northern wetlands under contemporary conditions.

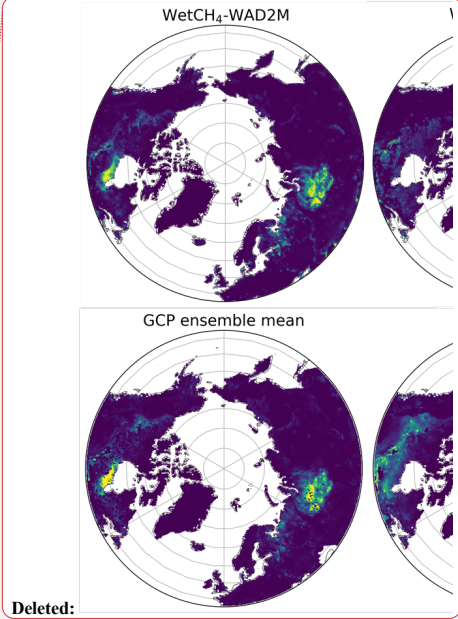
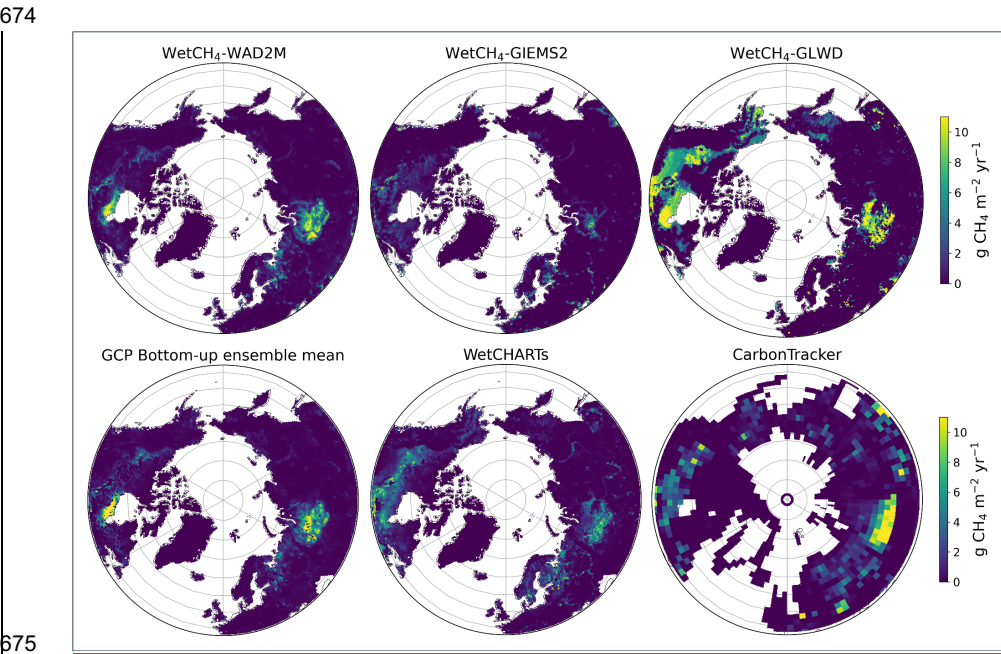


Fig. 6 Mean annual wetland CH₄ fluxes: the top row contains WetCH₄ upscaled fluxes between 2016 and 2022 and weighted by wetland fractions for three wetland maps WAD2Mv2, GIEMS2, and GLWDv1; the bottom row contains bottom-up GCP ensemble mean, WetCHARTs, and top-down estimates of CarbonTracker-CH₄ natural microbial emissions.

We compared spatial distributions of our upscaled fluxes (WetCH₄) with two alternative upscaled datasets. Using the same wetland weights, our product showed similar spatial patterns to UpCH₄ (McNicol et al., 2023) and the upscaled fluxes from Peltola et. al. (2019) (Fig. S9). Spatially, the maximum mean flux of 2016-2022 for WetCH₄ with WAD2Mv2 was 69 mg CH₄ m⁻² day⁻¹, UpCH₄ produced a maximum mean flux between 2016-2018 of 88 mg CH₄ m⁻² day⁻¹. While all three products predicted concentrated CH₄ exchange in the Hudson Bay Lowlands and West Siberian Lowlands, and low fluxes in West Canadian Arctic tundra, WetCH₄ predicted lower fluxes in forested wetlands of West Canada than UpCH₄ (Fig. S9 a,b). With GLWDv1, WetCH₄ predicted similar fluxes to those of Peltola et al. (2019), with the exception of a number of potent emitting grids in the West Siberian Lowlands (Fig. S9 c,d) and a maximum mean flux of 132 mg CH₄ m⁻² day⁻¹ from WetCH₄.

3.2.2 Seasonal cycles of wetland CH₄ emissions

Mean seasonal cycles of wetland CH₄ emissions were consistent with bottom-up estimates in the domain and top-down inversions in high latitudes (Fig. 7). The amplitudes of two ML-based estimates agreed in the domain (WetCH₄ and UpCH₄ both within WAD2Mv2 wetland areas) and were lower than the ensemble means of GCP or WetCHARTs estimates during the growing season (Fig. 7a). In the northern high latitudes (60° - 90° N), the amplitudes of this study closely agree with WetCHARTs, and both were lower than the ensemble means of GCP in the growing season (Fig. 7b). Our emissions in June-July-August were lower than the emissions attributed by the atmospheric inversion of CarbonTracker-CH₄, which does not discriminate between wetland and open water sources. We did not use comparisons with CarbonTracker-CH₄ for 45°-90° due to likely considerable contributions from aquatic systems and other non-wetland factors in the inversion estimates. Notably, uncertainties between ML-based approaches with the same wetland extents showed less variation than those between process-based models, especially during the growing season. The phase of our estimates (WetCH₄) agreed with bottom-up and top-down models, peaking in July followed by August (Fig. 7a,b), whereas UpCH₄ showed a month lag, probably due to the two- or three-week lag of predictor variables selected in UpCH₄ (McNicol et al., 2023). Peak fluxes in July and August were commonly seen in tower measurements.

The seasonality in upscaled wetland CH₄ emissions corresponded to the intensities of fluxes and dynamics of wetland areas. We compared mean seasonal cycles of upscaled products with different dynamic or static wetland maps to constrain the impacts of wetland areas (Fig. 7c). As observed in spatial distributions (Fig. 7a,c), emissions from the potential emitting surface (WetCH₄_GLWDv1) were 95% higher than those from reference inundated wetlands (WetCH₄_WAD2Mv2) during the growing season, and doubling in winter. Within the GLWDv1 emitting surface, WetCH₄ predicted higher emissions than Peltola et al. (2019) in July (43%),

August (43%), December (41%), and January (61%), but 15% lower in October. We decoupled the mean annual seasonal cycle for WAD2M from the emission seasonality by using a fixed maximum WAD2M extent. [The addition of maximum annual wetland extent further constrains the limitations of seasonal WAD2M extents in underestimating methane emitting surface for northern high latitude wetlands, especially in cold seasons.](#) The resulting seasonal emissions primarily driven by soil temperatures and moisture manifested elevated emissions in all months and an intensified seasonal cycle. Reported emissions ([Zona et al., 2016](#)) and large bursts (Mastepanov et al., 2008) from the freezing active layer at permafrost areas in October (zero-curtain period) may not be well captured by our ML model. The differences in wetland areas between the two dynamic products (WAD2Mv2 and GIEMS2) mostly affected emissions in May and June in WetCH₄, but significantly affected emission magnitudes in UpCH₄. Despite the differences in wetland areas, the phases of emissions cycles of WetCH₄ were consistent with those from Peltola et al., whereas UpCH₄ again lagged a month.

We compared upscaled seasonal cycles with CH₄ fluxes estimated from regional airborne measurements taken during CARVE campaigns over the Alaska North Slope (Fig. 7d). Given that the wetland area in this region is uncertain (Miller et al., 2016), we computed mean seasonal cycles over the land assuming all land in this area is water saturated in the soil, over freshwater wetlands of CALU, and over WAD2M and Hydrolakes, representing three different scenarios. In the lowland area of the North Slope (74295 km² spanning between 69.8°N - 71.4°N, 164.4°W - 152.7°W), the wetland area was estimated at 10611 km² from CALU, 4800 km² from GLWDv2, and 4049 km² from the maximum extent month in July of WAD2Mv2, respectively. The range of our upscaled estimates aligned with regional emissions derived from CARVE measurements. Chang et al. (2014) estimated 7 ± 2 mg CH₄ m⁻² d⁻¹ of mean CH₄ fluxes during the growing season in the North Slope from the column analysis of CARVE data. The mean fluxes (May to September) of WetCH₄ with CALU were estimated at 7.3 ± 0.8 mg CH₄ m⁻² d⁻¹ (5.5 ± 0.6 mgC CH₄ m⁻² d⁻¹), which is within the range of various CARVE estimations (Miller et al., 2016). The landscape is in the biome of the Arctic coastal tundra and is covered by sedges, grasses, mosses, and dwarf shrubs. A large number of lakes and freshwater ponds are scattered across the area. Studies at the West Alaska lowland of Yukon–Kuskokwim Delta found aquatic fluxes that were about ten times higher than in wet tundra during September (Ludwig et al., 2023), suggesting that a major source of the airborne fluxes missing in WetCH₄ in the late growing season, can be attributed to open water fluxes. Remarkable increases could be in summer and winter if we assume wetland over this region, as indicated by the range between the green and the black lines in Fig. 8d. Yet, future emissions due to permafrost thaw still depend on the hydrological changes of the landscape.

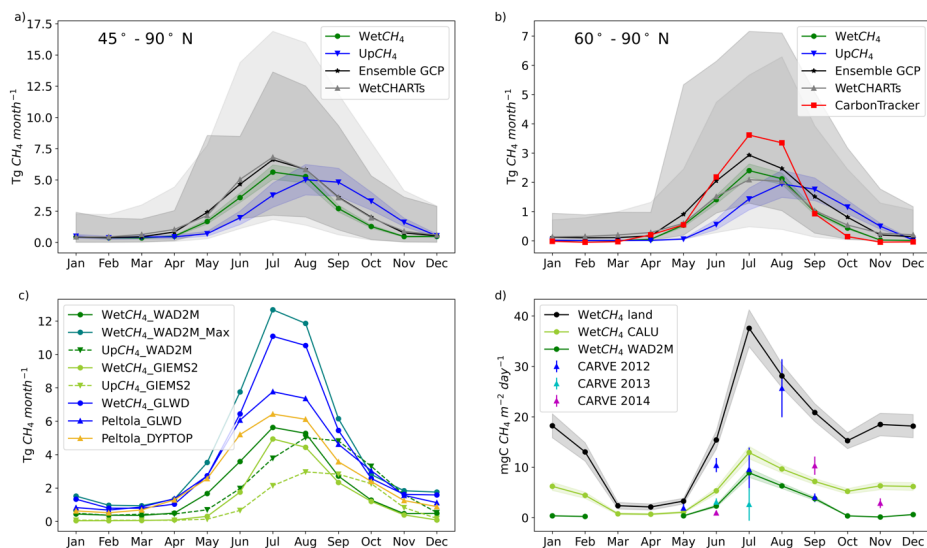
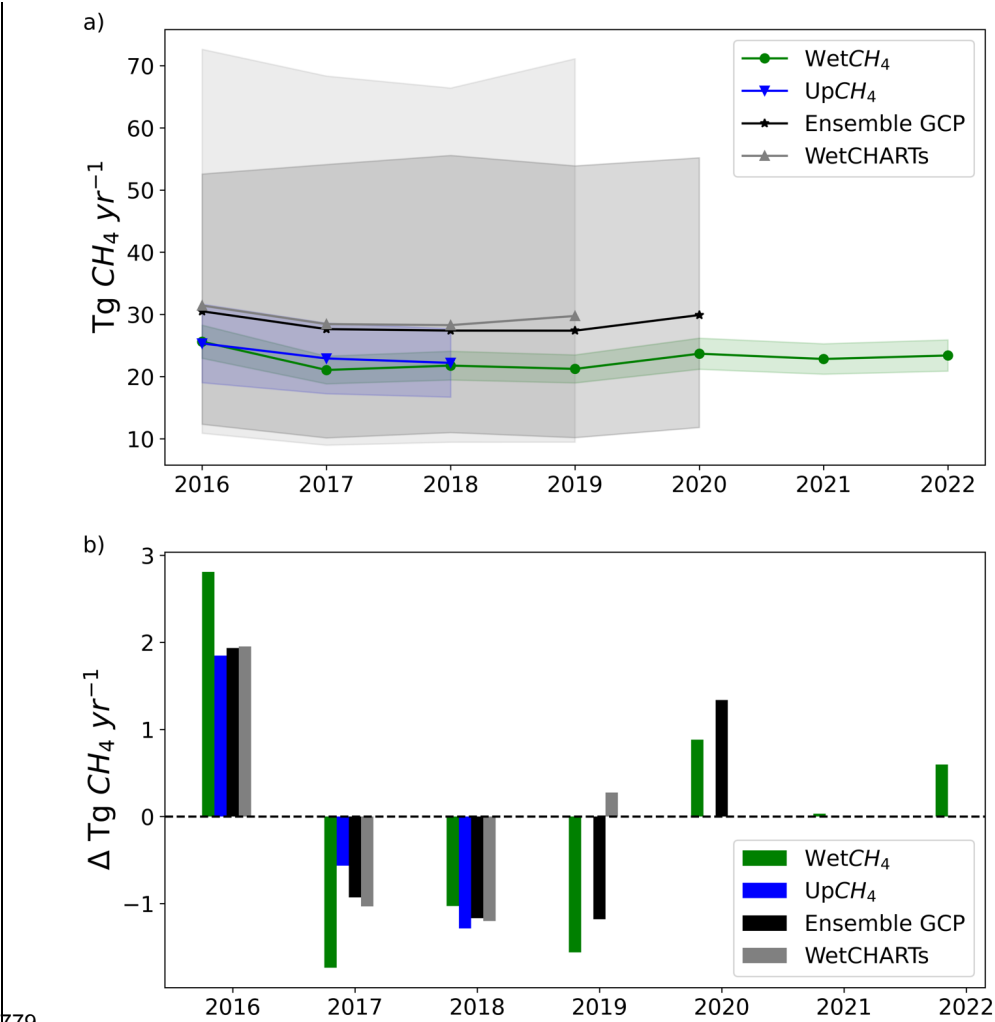


Fig. 7 Multi-year average seasonal cycles of wetland CH₄ emissions: (a) comparison of ML upscaled mean seasonal cycles in reference wetland areas (WAD2Mv2) with the cycles from process-based models in the northern mid-high latitudes (45° - 90° N); (b) same comparison for northern high latitudes (60° - 90° N) and addition of atmospheric CarbonTracker-CH₄ attributed microbial emissions (2016-2022); (c) comparison of three ML upscaled mean seasonal cycles of CH₄ emissions with different wetland area maps (WAD2Mv2, WAD2Mv2 maximum extent, GIEMS2, GLWDv1); (d) comparison of WetCH₄ mean seasonal cycles over the land (black line), weighted by wetland of the CALU map (olive line), or weighted by fractions of WAD2Mv2 (green line), with estimates of CH₄ fluxes in growing seasons from CARVE retrievals in North Slope area of Alaska (Zona et al., 2016).

3.2.3 Interannual variations in wetland CH₄ emissions

The mean annual emissions from ML-based estimates with WAD2M were lower than the GCP ensemble mean and WetCHARTs over different years from 2016 forward (Fig. 8a). All products demonstrated similar emission patterns for the domain in the interannual trends and variations, highest in 2016 and lower for three years from 2017 to 2019 (Fig. 8). The interannual variations in WetCH₄ were driven by the interannual variability in the upscaled fluxes as only multi-year mean seasonal dynamics from WAD2Mv2 were used. All products identified intensified emissions in 2016 as indicated by the variations relative to period means (Fig. 8b). Higher than

778 period average emissions in 2020 were also modeled by WetCH₄ and ensemble GCP.



779
780 Fig. 8 Wetland CH₄ a) annual emissions and associated uncertainties in colored shades and b)
781 variations relative to multi-year means in the research domain (45° - 90° N). Wetland area data
782 applied in WetCH₄ and UpCH₄ was WAD2Mv2. Time periods of multi-year means: WetCH₄
783 (2016-2022); UpCH₄ (2016-2018); GCP Bottom-up ensemble mean (2016-2020); WetCHARTs
784 (2016-2019).

785
786 Subregional annual emissions and interannual variability (Fig. 9) of WetCH₄ were calculated for
787 eight subregions in the northern high latitudes (Fig. S11): Siberian tundra, East Siberia, West

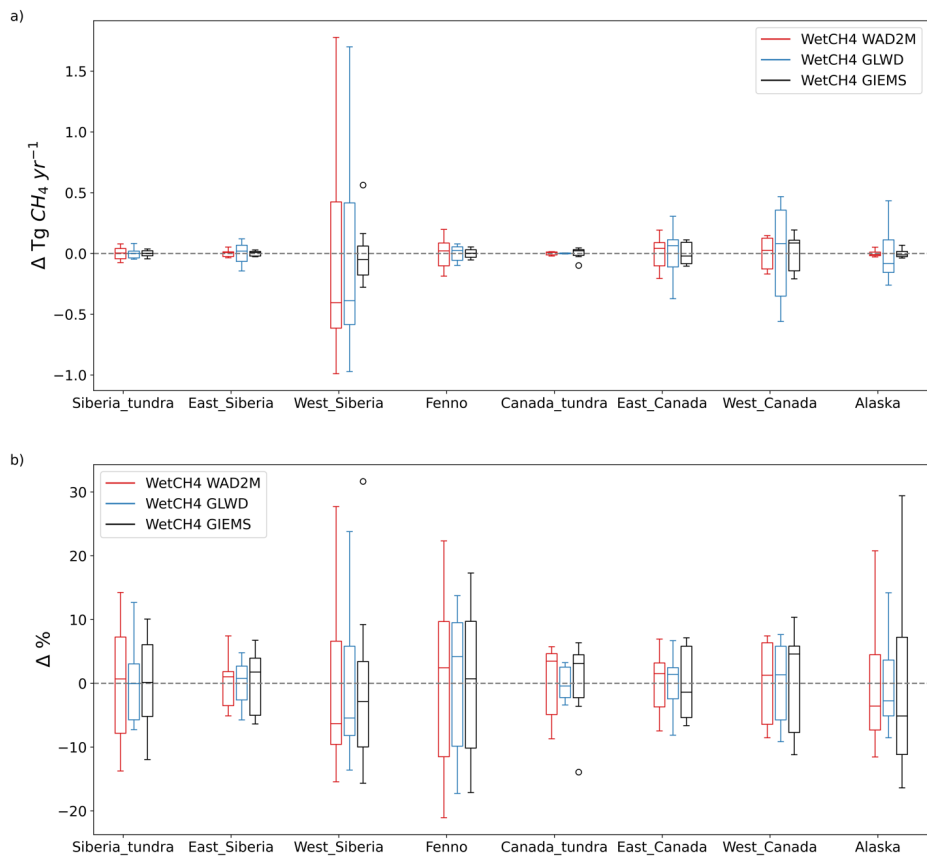
Deleted: The recent intensification from wetland emissions was discovered globally with an important contribution from northern wetlands (S. Peng et al., 2022; Yuan et al., 2024; Z. Zhang, Poulter, et al., 2023)....

Deleted: ¶

Deleted: E

Deleted: GCP

796 Siberia, Fennoscandia, Canadian tundra, East Canada, West Canada, and Alaska. The main
 797 differences in WetCH₄ estimated emissions between WAD2Mv2 and GLWDv1 occurred in the
 798 East Siberia, East Canada, West Canada, and Alaska subregions. However, interannual
 799 variabilities were similar. Interannual variations from West Siberia accounted for 51% the
 800 variations in domain emissions (Fig. 9a). The positive change in East Canada canceled the
 801 negative change in West Siberia in 2021, resulting in low variability in the domain emission for
 802 that year (Fig. 8). The relative interannual variability, which was calculated as the percentage of
 803 a subregional variation to its period mean, was attributed to those from West Siberia,
 804 Fennoscandia, West Canada, and Alaska (Fig. 9b).
 805



806
 807 Fig. 9 Interannual variations and variability in subregions predicted by WetCH₄ with WAD2Mv2,
 808 GLWDv1, and GIEMS2, respectively: (a) interannual variations with respect to period means
 809 (2016-2022); (b) relative variability as the percentage of its period mean. Delta in the y axis
 810 denotes the annual emissions minus mean annual emissions in the period 2016-2022. The

811 boxplots show the first quartile, the median, and the third quartile of the data with the whiskers
812 denoting the 1.5x interquartile range below/above the first/third quartile.

813 4. Discussion

814 This study provides new estimates of daily scale 10-km wetland CH₄ fluxes for the northern
815 terrestrial wetland region, upscaled from EC data. The upscaling framework was driven by
816 MERRA2 meteorological variables and soil temperatures and constrained by satellite products
817 from SMAP soil moisture and MODIS NBAR, resulting in a good prediction accuracy (mean R² =
818 0.70 and mean MAE = 27 nmol m⁻² s⁻¹) in monthly mean fluxes. Model agreement worsened at
819 daily and weekly timesteps due to higher variability in CH₄ fluxes at finer temporal resolutions. In
820 our framework, we applied a rigorous criterion on the counts of half-hourly observations to
821 control the selection quality of daily gap-filled data, which may filter out errors introduced by the
822 gap-filling process or lack of observations for calculating daily means. The improvement in
823 model performance can be partly attributed to the inclusion of soil temperature, satellite
824 assimilation of soil moisture, and MODIS vegetation reflectance in the framework that
825 represents controlling factors or proxies of CH₄ fluxes recognized in field experiments and
826 synthesis studies (Fig. 3).
827

828 4.1 Important drivers to improve RF model predictive performance

829 Soil temperature plays an important role in microbial growth and dormancy (Chadburn et al.,
830 2020), and exponentially affects microbial CH₄ emission rates although the temperature
831 sensitivity varies across space and time (Knox et al., 2021; van Hulzen et al., 1999). In northern
832 wetlands, soil temperature is often more spatially variable relative to air temperature due to
833 snow insulation and active layer depth (Smith et al., 2022; W. Wang et al., 2016; Yuan et al.,
834 2022), and thus should be considered in upscaling models. Compared to air temperature or land
835 surface temperature that were used in previous upscaling studies (Peltola et al., 2019; McNicol
836 et al., 2023), the inclusion of MERRA2 soil temperatures in WetCH₄ likely contributed to a higher
837 model predictive performance, although the impact of scale mismatch between the native
838 MERRA2 spatial resolution and the local footprints on the upscaled fluxes were not quantified.
839 Independent validation studies found significant correlations in the temporal trend and seasonal
840 cycles between MERRA2 soil temperatures and *in situ* observations (M. Li et al., 2020; Ma et
841 al., 2021) in the U.S. and mid-latitude Eurasia. However, lower correlations and overestimated
842 monthly variability were found in the cold season in Pan-Arctic (Herrington et al., 2022). This
843 suggests the impact of the uncertainty in MERRA2 soil temperatures were concentrated in the
844 cold season, when CH₄ fluxes were low. The agreement between ensemble means of soil
845 temperatures from eight reanalysis and land data assimilation system products and station
846 measurements improved in the pan-Arctic region (Herrington et al., 2022), suggesting the
847 potential to reduce upscaling uncertainty forced by the ensemble mean of reanalysis datasets.
848

Emergent vegetation with aerenchyma affects the recent substrate availability and the plant-mediated transport of CH₄ (Kyzivat et al., 2022; Melack & Hess, 2023). We used the full land bands of the MODIS NBAR product rather than derived vegetation indices used in previous upscaling studies, as signals indicating wetland vegetation functional characteristics may be lost when merging bands to derive simple vegetation indices (Chen et al., 2013). In our study, the near-infrared and shortwave infrared bands (NBAR bands 2, 5, and 7) presented relatively high importance in the RF model due to their associations with vegetation characteristics and water table dynamics in northern peatlands (Baskaran et al., 2022; Burdun et al., 2023). Satellite inputs provide high spatial resolution constraints on the environmental variability and help reduce model spatial predictive errors (Fig. 3), indicating the requirement of high spatial resolution driving input for accurately modeling wetland CH₄ fluxes (Elder et al., 2021).

Surface and rootzone soil moisture are important controls on ecosystem anaerobic metabolism. Low soil moisture implies aerobic conditions and allows methanotrophic bacteria to consume CH₄, whereas high soil moisture enables CH₄ production and suppresses consumption (Liebner et al., 2011; Olefeldt et al., 2013; Spahni et al., 2011). Soil wetness estimated in the rootzone and the profile from SMAP measurements may be able to capture water table dynamics and hence ranked as important in WetCH₄ model performance. Validation of the SMAP level 4 soil moisture data assimilation product has shown that it meets the performance requirement of unbiased root-mean-square error <0.04 m³/m³ (Colliander et al., 2022). However, the validation sites are mostly located in North American grassland, cropland and shrubland, requiring more *in situ* soil moisture observations in high latitude tundra and peatland. Regional validation studies suggested uncertainties of satellite derived soil moisture including SMAP at high latitudes were high (Högström et al., 2018; Wrona et al., 2017) and remained to be addressed.

Underground processes of CH₄ production and oxidation are difficult to model (Ueyama, Knox, et al., 2023), especially for seasonal cycles in the northern high latitudes. A hysteresis effect that manifests intra-seasonal variability in the dependence of CH₄ fluxes on temperature has been observed at EC sites (K.-Y. Chang et al., 2021), but it was not reproduced in WetCH₄. Positive hysteresis and the difference in frozen status from topsoil to deep soil during autumn freeze results in zero curtain periods that have been observed at high latitude tundra (Bao et al., 2021; Zona et al., 2016), the occurrence of which was subsequently underestimated in our model.

The amount of additional substrate available for methanogenesis due to soil freezing/thawing, missing in our framework, could be a controlling factor of the occurrence of this phenomenon. Higher substrate availability elevates methanogen abundance and activities during autumn freeze (Bao et al., 2021). However, spatially explicit substrate data are not available. Using proxies such as net primary production or EVI for substrate availability might be oversimplified (Larmola et al., 2010; T. Li et al., 2016; Peltola et al., 2019). In addition, the uncertainty of deep soil temperature of training inputs in late autumn may hinder the model's ability to capture patterns of high emissions during zero curtain periods observed at Alaska tundra (Fig. S10). More temporally accurate soil temperature data is needed to delineate the soil freezing progress and properly constrain predictions of CH₄ emission during the cold season (Arndt et al., 2019).

893 The UpCH₄ results (McNicol et al., 2023) also suggest that simply imposing lags to temporal
894 predictors in RF cannot capture complex intra-seasonal variability due to the complicated lag
895 effects interacting with the water table depth (Turner et al., 2021). Without timestamps in
896 predictors, RF treats time series fluxes independently, which may limit its predictive
897 performance. Deep learning models designed to account for temporal progress in data, such as
898 Long Short Term Memory (LSTM) neural networks, may improve modeling accuracy of
899 seasonal cycles (Reichstein et al., 2019; Yuan et al., 2022).
900

901 **4.2 Data limitations in current EC CH₄ observations**

902 Data deficiency in EC CH₄ flux observations in winter and in under-represented areas limited the
903 RF model's extrapolation ability. Data abundance and representativeness across space, time,
904 and wetland types drives model performance and ability to extrapolate for the data-driven
905 approach. The 26 wetland EC sites included in this study are largely located in Fennoscandia,
906 East Canada and Alaska (Fig. 2), leaving some regional emission hotspots under-represented.
907 For instance, Western Siberian Lowlands, the large wetland complex and the major contributor
908 of interannual variations of CH₄ in the region, has little data. The nearest site (RU-VRK, not
909 included in this study due to the observations before our study period) is situated on the western
910 side of the Ural mountains, within the Usa River Depression. Cold season emissions could
911 contribute a substantial fraction of the Arctic tundra annual CH₄ budget (Mastepanov et al.,
912 2008; Mavrovic et al., 2024; Zona et al., 2016). But after filtering, 23% of the EC data in high
913 latitudes (>60° N) were recorded between November and March, which could be insufficient for
914 accurately modeling and upscaling zero curtain period fluxes.
915

916 Ten bog and fen sites used for modeling contain all season daily flux records with more than 11
917 half-hourly observations per day, all from Fennoscandia and Canada. Although Alaska is
918 represented by 11 wetland sites, sufficient winter observations with good quality are still
919 needed. West Siberian Lowlands are underrepresented by EC CH₄ sites. Missing data in
920 MODIS NBAR due to snow cover or gaps in SMAP reduced training data by 31% and 48% in
921 the study domain, respectively. Filling data of MODIS NBAR to account for snow cover
922 information and gap-filling SMAP soil moisture products can make full use of available EC
923 observations and help improve model performance in cold seasons. Since gaps in winter SMAP
924 data were filled with zero values, our approach has limitations in the estimation in winter soil
925 moisture gaps in areas where zero curtain and talik were not represented by our interpolated
926 soil temperatures, for example, in coastal areas.
927

928 Many wetland sites in the study are located in areas with peatland presence, with 35% of sites
929 in peatland-rich areas with >50% peatland cover (Hugelius et al., 2020). Mineral soil (soil
930 containing less than 12% organic carbon by weight) marshes, though covering only 5% of the
931 total wetland area in the northern high latitudes, need to be considered when deploying new EC
932 sites due to their high CH₄ emissions (Kuhn et al., 2021; Olefeldt et al., 2021). This study
933 identified regional CH₄ emission hotspots and areas undergoing strong interannual variations,
934 which are yet not part of the current FLUXNET network. However, the 10 km resolution of the

Deleted: limited

Deleted: that is compiled from a single

RF estimates prohibits the identification of local hotspots that may occur at <1-10 m scales (Elder et al., 2021). The wall-to-wall flux maps also provide spatially continuous information for effectively further developing the CH₄ flux tower network.

4.3 Budget comparison

WetCH₄ estimated annual and seasonal mean emissions that were comparable to existing data-driven products in the study domain (Table S3). With the dynamic WAD2Mv2 map, our estimation was 0.7 Tg CH₄ yr⁻¹ smaller than UpCH₄ due to the mean seasonal cycles between 2010 and 2020 from WAD2M applied in our estimation. With the same static GLWDv1 map, our estimation was about 22% larger than the estimate from Peltola et al. (37.5 ± 12 Tg CH₄ yr⁻¹ for 2013-2014) despite the different periods. This is attributed to higher fluxes estimated by WetCH₄ in DJF and JJA seasons. With two versions of the static GLWD maps, we estimated potential annual emissions between 46.0 and 51.6 Tg CH₄ yr⁻¹. Compared to GLWDv1, version 2 of GLWD mapped smaller wetland fractions in the Hudson Bay Lowlands with intense CH₄ fluxes and more wetlands in the northwest of the Ural Mountains, Eastern Siberia, and the Sanjiang Plain, where CH₄ intensities were weaker, resulting in a larger estimate of the annual emission (Fig. S13). The wide range of data-driven estimates was driven by the differences in wetland maps. While WAD2M provides crucial information on wetland inundation dynamics controlling interannual and inter-seasonal changes in CH₄ emitting areas, areas with saturated soil in the Arctic tundra are likely severely underestimated (Fig. 7d), requiring more accurate maps delineating wet tundra communities at higher spatial resolution (e.g., < 1 km). Incorporating wetland fractions derived from high-resolution thematic maps (e.g., CALU) can improve the use of WAD2M in cold regions. Developing/improving higher resolution microwave remote sensing products capable of tracking dynamic changes in local soil moisture conditions is also needed. Together, these two components likely currently yield the largest sources of uncertainty in high latitude terrestrial CH₄ budgets.

Bottom-up estimates on wetland CH₄ emissions from data-driven, GCP ensemble means and WetCHARTs are smaller than the top-down CarbonTracker-CH₄ estimate on natural microbial emissions because the latter includes emissions from aquatic systems. Aquatic CH₄ emissions for this region have been estimated at 5.5 Tg CH₄ yr⁻¹ from rivers and streams (Rocher-Ros et al., 2023) and 16.6 Tg CH₄ yr⁻¹ from lakes (Johnson et al., 2022). The total emissions budget for wetlands and open water, based on this study and the aquatic estimates, are about 44.9 Tg CH₄ yr⁻¹, which is 4 Tg CH₄ yr⁻¹ more than the CarbonTracker-CH₄ estimate. The amplitudes of WetCH₄ seasonal mean fluxes align with bottom up and top down estimates. Differences in the seasonal dynamics of wetland maps are the major source of upscaling uncertainty and result in various uncertainties between regional estimates. While atmospheric inversion models need bottom-up estimates as priors, data-driven upscaled CH₄ products offer alternatives to process-based estimates to assist with inversion models in regions where data-driven models perform well (Bloom et al., 2017; Melton et al., 2013).

Deleted: 8

4.4 Future directions

Future development of EC networks in the northern high latitudes is urgently needed to provide additional observations needed to improve model-based upscaling of CH₄ flux budgets, and to address current gaps in ecosystem and regional representation. Deploying new sites in under-represented areas will not only benefit flux upscaling efforts but also our understanding of how ecosystem metabolism responds to the changing climate (Baldocchi, 2020; Pallandt et al., 2022; Villarreal & Vargas, 2021). With the availability of long-term predictor variable data, it is possible to expand upscaling frameworks over longer periods (e.g., 2000 to current), when adequate flux observations in 2000-2010 from chambers are compiled, as 96% of the data were recorded after 2010 in FLUXNET-CH₄ (McNicol et al., 2023).

Several data products exist for the meteorological predictor variables. Quantifying measurement uncertainties between products of predictor variables and how the uncertainties propagate to upscaling products need to be addressed in future work. The mismatch of spatial scales between tower footprints and predictor variables may cause underestimation of abruptly high fluxes measured at tower landscapes when environmental conditions are averaged over half-degree grids (Chu et al., 2021; McNicol et al., 2023). Therefore, downscaling predictor variables for developing higher-resolution products is needed, especially for the Arctic region where thermokarst development is shaping permafrost landscapes with fragments of wetlands, thermokarst ponds, and forests (Miner et al., 2022; Osterkamp et al., 2000; Wik et al., 2016). For example, Fang et al. (2022) have downscaled global SMAP surface soil moisture to 1-km resolution, and Optical/Thermal and microwave fusion methods have been developed to downscale soil moisture (J. Peng et al., 2017). Nevertheless, downscaled products for rootzone or profile soil moisture are needed for upscaling CH₄ fluxes as are soil temperature products.

Beyond the ML-based upscaling framework, hybrid modeling of the data-driven approach and process-based models is a promising but also challenging direction of future study (Reichstein et al., 2019). One practice constrained regional data-driven fluxes with top-down estimates via auto-learned weights on per pixel fluxes in a region (Upton et al., 2023). Another practice pre-trained a time-dependent ML algorithm with initialization from process-based synthetic data and then fine-tuned the model with observations (Liu et al., 2022). Finally, leveraging physical constraints to increase the interpretability of data-driven models and computation efficiency is still an important factor to consider in all hybrid modeling.

5. Code and data availability

The daily CH₄ flux intensities in the northern wetlands at a spatial resolution of 0.098° x 0.098° and associated uncertainties, along with daily emissions weighted by WAD2M, GIEMS2, and GLWDv1, can be accessed through <https://doi.org/10.5281/zenodo.10802153> (Ying et al., 2024). Source code of ML modeling and upscaling is publicly available at <https://github.com/qclearwater/WetCH4.git>. Half-hourly EC data is available for download at <https://fluxnet.org/data/fluxnet-ch4-community-product/> (Delwiche et al., 2021).

1019 6. Conclusions

1020 We developed an ML framework (WetCH₄) to upscale daily wetland CH₄ fluxes of mid-high
1021 northern latitudes at 10-km spatial resolution combining EC tower measurements with satellite
1022 observations and climate reanalysis. WetCH₄ is novel in that it is the first upscaling framework to
1023 introduce SMAP soil moisture and MODIS reflectance in modeling wetland CH₄ fluxes to
1024 improve accuracy (mean $R^2 = 0.70$). The remote-sensing products provided high spatial
1025 resolution constraints associated with the abiotic controllers of CH₄ fluxes, indicating the
1026 importance of using high spatial resolution inputs in models for accurately simulating the
1027 spatiotemporally variable CH₄ emissions from heterogeneous northern wetland landscapes. The
1028 framework highlights the importance of soil temperature, vegetation, and soil moisture for
1029 modeling CH₄ fluxes in a data-driven approach. Using WetCH₄, an average annual CH₄
1030 emissions of $22.8 \pm 2.4 \text{ Tg CH}_4 \text{ yr}^{-1}$ with WAD2Mv2 was estimated and ranged between 15.7
1031 $\pm 1.8 \text{ Tg CH}_4 \text{ yr}^{-1}$ with GIEMS2 and $51.6 \pm 2.2 \text{ Tg CH}_4 \text{ yr}^{-1}$ with GLWDv2 from vegetated wetlands
1032 ($>45^\circ \text{ N}$) for 2016-2022, approximately 14-32% of the global wetland CH₄ budget (Saunio et
1033 al., 2020). Differences in estimates of wetland CH₄ emissions due to different wetland maps
1034 applied, highlighting the need for high resolution wetland maps and accurate delineation of wet
1035 soil dynamics. Emissions were relatively lower in 2017-2019 and intensified in 2016, 2020 and
1036 2022, with the largest interannual variations coming from West Siberia. Spatio-temporal
1037 distributions of CH₄ fluxes find emission hotspots and regions of intensified interannual
1038 variations that are not currently measured with EC. Comparing with current EC sites, we
1039 suggest a need for tower observations in wetlands of West Siberia and West Canada and
1040 diversified observations across wetland types. More site observations in soil water related
1041 variables are needed for improved understanding of flux controls in northern wetland
1042 ecosystems. Future wetland CH₄ upscaling work could benefit from improved soil moisture
1043 products and hybrid modeling.
1044

1045 Acknowledgements

1046 This work was supported by funding catalyzed by the TED Audacious Project (Permafrost
1047 Pathways). Resources supporting this work were provided by the NASA High-End Computing
1048 (HEC) Program through the NASA Center for Climate Simulation (NCCS) at Goddard Space
1049 Flight Center. We thank Sara Knox and Gavin McNicol for their helpful suggestions in the early
1050 stages of the compilation of EC CH₄ fluxes and the development of the upscaling product,
1051 respectively. Ben Poulter acknowledges support from the NASA Terrestrial Ecology Program.
1052 Annett Bartsch was supported by the European Space Agency CCI+ Permafrost and AMPAC-
1053 Net projects. Aram Kalhori was supported by the European Union's Horizon Europe program,
1054 grant agreement no. 101056848.

References

- Alonso, A., Muñoz-Carpena, R., & Kaplan, D. (2020). Coupling high-resolution field monitoring and MODIS for reconstructing wetland historical hydroperiod at a high temporal frequency. *Remote Sensing of Environment*, 247, 111807. <https://doi.org/10.1016/j.rse.2020.111807>
- Amatulli, G., McInerney, D., Sethi, T., Strobl, P., & Domisch, S. (2020). Geomorpho90m, empirical evaluation and accuracy assessment of global high-resolution geomorphometric layers. *Scientific Data*, 7(1), Article 1. <https://doi.org/10.1038/s41597-020-0479-6>
- Arndt, K. A., Oechel, W. C., Goodrich, J. P., Bailey, B. A., Kalhori, A., Hashemi, J., Sweeney, C., & Zona, D. (2019). Sensitivity of Methane Emissions to Later Soil Freezing in Arctic Tundra Ecosystems. *Journal of Geophysical Research: Biogeosciences*, 124(8), 2595–2609. <https://doi.org/10.1029/2019JG005242>
- Aydin, M., Verhulst, K. R., Saltzman, E. S., Battle, M. O., Montzka, S. A., Blake, D. R., Tang, Q., & Prather, M. J. (2011). Recent decreases in fossil-fuel emissions of ethane and methane derived from firn air. *Nature*, 476(7359), Article 7359. <https://doi.org/10.1038/nature10352>
- Baldocchi, D. D. (2003). Assessing the eddy covariance technique for evaluating carbon dioxide exchange rates of ecosystems: Past, present and future. *Global Change Biology*, 9(4), 479–492. <https://doi.org/10.1046/j.1365-2486.2003.00629.x>
- Baldocchi, D. D. (2020). How eddy covariance flux measurements have contributed to our understanding of Global Change Biology. *Global Change Biology*, 26(1), 242–260. <https://doi.org/10.1111/gcb.14807>
- Bansal, S., Creed, I. F., Tangen, B. A., Bridgman, S. D., Desai, A. R., Krauss, K. W., Neubauer, S. C., Noe, G. B., Rosenberry, D. O., Trettin, C., Wickland, K. P., Allen, S. T., Arias-Ortiz, A., Armitage, A. R., Baldocchi, D., Banerjee, K., Bastviken, D., Berg, P., Bogard, M. J., ... Zhu, X. (2023). Practical Guide to Measuring Wetland Carbon Pools and Fluxes. *Wetlands*, 43(8), 105. <https://doi.org/10.1007/s13157-023-01722-2>
- Bao, T., Xu, X., Jia, G., Billesbach, D. P., & Sullivan, R. C. (2021). Much stronger tundra methane emissions during autumn freeze than spring thaw. *Global Change Biology*, 27(2), 376–387. <https://doi.org/10.1111/gcb.15421>
- Baray, S., Jacob, D. J., Maasakkers, J. D., Sheng, J.-X., Sulprizio, M. P., Jones, D. B. A., Bloom, A. A., & McLaren, R. (2021). Estimating 2010–2015 anthropogenic and natural methane emissions in Canada using ECCO surface and GOSAT satellite observations. *Atmospheric Chemistry and Physics*, 21(23), 18101–18121. <https://doi.org/10.5194/acp-21-18101-2021>
- Bartsch, A., Efimova, A., Widhalm, B., Muri, X., von Baeckmann, C., Bergstedt, H., Ermokhina, K., Hugelius, G., Heim, B., & Leibmann, M. (2023). *Circumpolar Landcover Units* (1.0) [dataset]. Zenodo. <https://doi.org/10.5281/zenodo.8399018>
- Beaulieu, J. J., Waldo, S., Balz, D. A., Barnett, W., Hall, A., Platz, M. C., & White, K. M. (2020). Methane and Carbon Dioxide Emissions From Reservoirs: Controls and Upscaling. *Journal of Geophysical Research: Biogeosciences*, 125(12), e2019JG005474. <https://doi.org/10.1029/2019JG005474>

1098 Bergamaschi, P., Houweling, S., Segers, A., Krol, M., Frankenberg, C., Scheepmaker, R. A.,
1099 Dlugokencky, E., Wofsy, S. C., Kort, E. A., Sweeney, C., Schuck, T., Brenninkmeijer, C.,
1100 Chen, H., Beck, V., & Gerbig, C. (2013). Atmospheric CH₄ in the first decade of the 21st
1101 century: Inverse modeling analysis using SCIAMACHY satellite retrievals and NOAA
1102 surface measurements. *Journal of Geophysical Research: Atmospheres*, 118(13), 7350–
1103 7369. <https://doi.org/10.1002/jgrd.50480>
1104 Bloom, A. A., Bowman, K. W., Lee, M., Turner, A. J., Schroeder, R., Worden, J. R., Weidner, R.,
1105 McDonald, K. C., & Jacob, D. J. (2017). A global wetland methane emissions and
1106 uncertainty dataset for atmospheric chemical transport models (WetCHARTs version
1107 1.0). *Geoscientific Model Development*, 10(6), 2141–2156. [https://doi.org/10.5194/gmd-](https://doi.org/10.5194/gmd-10-2141-2017)
1108 10-2141-2017
1109 Bloom, A. A., Palmer, P. I., Fraser, A., Reay, D. S., & Frankenberg, C. (2010). Large-Scale
1110 Controls of Methanogenesis Inferred from Methane and Gravity Spaceborne Data.
1111 *Science*, 327(5963), 322–325. <https://doi.org/10.1126/science.1175176>
1112 Bodesheim, P., Jung, M., Gans, F., Mahecha, M. D., & Reichstein, M. (2018). Upscaled diurnal
1113 cycles of land–atmosphere fluxes: A new global half-hourly data product. *Earth System*
1114 *Science Data*, 10(3), 1327–1365. <https://doi.org/10.5194/essd-10-1327-2018>
1115 Breiman, L. (2001). Random Forests. *Machine Learning*, 45(1), 5–32.
1116 <https://doi.org/10.1023/A:1010933404324>
1117 Bruhwiler, L., Dlugokencky, E., Masarie, K., Ishizawa, M., Andrews, A., Miller, J., Sweeney, C.,
1118 Tans, P., & Worthy, D. (2014). CarbonTracker-CH₄: An assimilation system for
1119 estimating emissions of atmospheric methane. *Atmospheric Chemistry and Physics*,
1120 14(16), 8269–8293. <https://doi.org/10.5194/acp-14-8269-2014>
1121 Burdun, I., Bechtold, M., Aurela, M., De Lannoy, G., Desai, A. R., Humphreys, E., Kareksela, S.,
1122 Komisarenko, V., Liimatainen, M., Marttila, H., Minkinen, K., Nilsson, M. B., Ojanen, P.,
1123 Salko, S.-S., Tuittila, E.-S., Uuemaa, E., & Rautiainen, M. (2023). Hidden becomes
1124 clear: Optical remote sensing of vegetation reveals water table dynamics in northern
1125 peatlands. *Remote Sensing of Environment*, 296, 113736.
1126 <https://doi.org/10.1016/j.rse.2023.113736>
1127 Chadburn, S. E., Aalto, T., Aurela, M., Baldocchi, D., Biasi, C., Boike, J., Burke, E. J., Comyn-
1128 Platt, E., Dolman, A. J., Duran-Rojas, C., Fan, Y., Friborg, T., Gao, Y., Gedney, N.,
1129 Göckede, M., Hayman, G. D., Holl, D., Hugelius, G., Kutzbach, L., ... Westermann, S.
1130 (2020). Modeled Microbial Dynamics Explain the Apparent Temperature Sensitivity of
1131 Wetland Methane Emissions. *Global Biogeochemical Cycles*, 34(11), e2020GB006678.
1132 <https://doi.org/10.1029/2020GB006678>
1133 Chang, K.-Y., Riley, W. J., Knox, S. H., Jackson, R. B., McNicol, G., Poulter, B., Aurela, M.,
1134 Baldocchi, D., Bansal, S., Bohrer, G., Campbell, D. I., Cescatti, A., Chu, H., Delwiche, K.
1135 B., Desai, A. R., Euskirchen, E., Friborg, T., Goeckede, M., Helbig, M., ... Zona, D.
1136 (2021). Substantial hysteresis in emergent temperature sensitivity of global wetland CH₄
1137 emissions. *Nature Communications*, 12(1), Article 1. [https://doi.org/10.1038/s41467-021-](https://doi.org/10.1038/s41467-021-22452-1)
1138 22452-1
1139 Chang, R. Y.-W., Miller, C. E., Dinardo, S. J., Karion, A., Sweeney, C., Daube, B. C.,
1140 Henderson, J. M., Mountain, M. E., Eluszkiewicz, J., Miller, J. B., Bruhwiler, L. M. P., &
1141 Wofsy, S. C. (2014). Methane emissions from Alaska in 2012 from CARVE airborne

1142 observations. *Proceedings of the National Academy of Sciences*, 111(47), 16694–
 1143 16699. <https://doi.org/10.1073/pnas.1412953111>
 1144 Chen, Y., Huang, C., Ticehurst, C., Merrin, L., & Thew, P. (2013). An Evaluation of MODIS Daily
 1145 and 8-day Composite Products for Floodplain and Wetland Inundation Mapping.
 1146 *Wetlands*, 33(5), 823–835. <https://doi.org/10.1007/s13157-013-0439-4>
 1147 Choe, H., Chi, J., & Thorne, J. H. (2021). Mapping Potential Plant Species Richness over Large
 1148 Areas with Deep Learning, MODIS, and Species Distribution Models. *Remote Sensing*,
 1149 13(13), Article 13. <https://doi.org/10.3390/rs13132490>
 1150 Chu, H., Luo, X., Ouyang, Z., Chan, W. S., Dengel, S., Biraud, S. C., Torn, M. S., Metzger, S.,
 1151 Kumar, J., Arain, M. A., Arkebauer, T. J., Baldocchi, D., Bernacchi, C., Billesbach, D.,
 1152 Black, T. A., Blanken, P. D., Bohrer, G., Bracho, R., Brown, S., ... Zona, D. (2021).
 1153 Representativeness of Eddy-Covariance flux footprints for areas surrounding AmeriFlux
 1154 sites. *Agricultural and Forest Meteorology*, 301–302, 108350.
 1155 <https://doi.org/10.1016/j.agrformet.2021.108350>
 1156 Colliander, A., Reichle, R. H., Crow, W. T., Cosh, M. H., Chen, F., Chan, S., Das, N. N.,
 1157 Bindlish, R., Chaubell, J., Kim, S., Liu, Q., O'Neill, P. E., Dunbar, R. S., Dang, L. B.,
 1158 Kimball, J. S., Jackson, T. J., Al-Jassar, H. K., Asanuma, J., Bhattacharya, B. K., ...
 1159 Yueh, S. H. (2022). Validation of Soil Moisture Data Products From the NASA SMAP
 1160 Mission. *IEEE Journal of Selected Topics in Applied Earth Observations and Remote*
 1161 *Sensing*, 15, 364–392. <https://doi.org/10.1109/JSTARS.2021.3124743>
 1162 Davidson, S. J., Santos, M. J., Sloan, V. L., Reuss-Schmidt, K., Phoenix, G. K., Oechel, W. C.,
 1163 & Zona, D. (2017). Upscaling CH₄ Fluxes Using High-Resolution Imagery in Arctic
 1164 Tundra Ecosystems. *Remote Sensing*, 9(12), Article 12.
 1165 <https://doi.org/10.3390/rs9121227>
 1166 Delwiche, K. B., Knox, S. H., Malhotra, A., Fluet-Chouinard, E., McNicol, G., Feron, S., Ouyang,
 1167 Z., Papale, D., Trotta, C., Canfora, E., Cheah, Y.-W., Christianson, D., Alberto, M. C. R.,
 1168 Alekseychik, P., Aurela, M., Baldocchi, D., Bansal, S., Billesbach, D. P., Bohrer, G., ...
 1169 Jackson, R. B. (2021). FLUXNET-CH₄: A global, multi-ecosystem dataset and analysis
 1170 of methane seasonality from freshwater wetlands. *Earth System Science Data*, 13(7),
 1171 3607–3689. <https://doi.org/10.5194/essd-13-3607-2021>
 1172 Entekhabi, D., Njoku, E. G., O'Neill, P. E., Kellogg, K. H., Crow, W. T., Edelstein, W. N., Entin,
 1173 J. K., Goodman, S. D., Jackson, T. J., Johnson, J., Kimball, J., Piepmeier, J. R., Koster,
 1174 R. D., Martin, N., McDonald, K. C., Moghaddam, M., Moran, S., Reichle, R., Shi, J.
 1175 C., ... Van Zyl, J. (2010). The Soil Moisture Active Passive (SMAP) Mission.
 1176 *Proceedings of the IEEE*, 98(5), 704–716. <https://doi.org/10.1109/JPROC.2010.2043918>
 1177 Euskirchen, E. S., Edgar, C. W., Kane, E. S., Waldrop, M. P., Neumann, R. B., Manies, K. L.,
 1178 Douglas, T. A., Dieleman, C., Jones, M. C., & Turetsky, M. R. (2024). Persistent net
 1179 release of carbon dioxide and methane from an Alaskan lowland boreal peatland
 1180 complex. *Global Change Biology*, 30(1), e17139. <https://doi.org/10.1111/gcb.17139>
 1181 Fang, B., Lakshmi, V., Cosh, M., Liu, P.-W., Bindlish, R., & Jackson, T. J. (2022). A global 1-km
 1182 downscaled SMAP soil moisture product based on thermal inertia theory. *Vadose Zone*
 1183 *Journal*, 21(2), e20182. <https://doi.org/10.1002/vzj2.20182>
 1184 Feron, S., Malhotra, A., Bansal, S., Fluet-Chouinard, E., McNicol, G., Knox, S. H., Delwiche, K.
 1185 B., Cordero, R. R., Ouyang, Z., Zhang, Z., Poulter, B., & Jackson, R. B. (2024). Recent

1186 increases in annual, seasonal, and extreme methane fluxes driven by changes in climate
 1187 and vegetation in boreal and temperate wetland ecosystems. *Global Change Biology*,
 1188 30(1), e17131. <https://doi.org/10.1111/gcb.17131>
 1189 Friedlingstein, P., Jones, M. W., O'Sullivan, M., Andrew, R. M., Bakker, D. C. E., Hauck, J., Le
 1190 Quéré, C., Peters, G. P., Peters, W., Pongratz, J., Sitch, S., Canadell, J. G., Ciais, P.,
 1191 Jackson, R. B., Alin, S. R., Anthoni, P., Bates, N. R., Becker, M., Bellouin, N., ... Zeng,
 1192 J. (2022). Global Carbon Budget 2021. *Earth System Science Data*, 14(4), 1917–2005.
 1193 <https://doi.org/10.5194/essd-14-1917-2022>
 1194 Gelaro, R., McCarty, W., Suárez, M. J., Todling, R., Molod, A., Takacs, L., Randles, C. A.,
 1195 Darmenov, A., Bosilovich, M. G., Reichle, R., Wargan, K., Coy, L., Cullather, R., Draper,
 1196 C., Akella, S., Buchard, V., Conaty, A., Silva, A. M. da, Gu, W., ... Zhao, B. (2017). The
 1197 Modern-Era Retrospective Analysis for Research and Applications, Version 2 (MERRA-
 1198 2). *Journal of Climate*, 30(14), 5419–5454. <https://doi.org/10.1175/JCLI-D-16-0758.1>
 1199 Heimann, M. (2011). Enigma of the recent methane budget. *Nature*, 476(7359), Article 7359.
 1200 <https://doi.org/10.1038/476157a>
 1201 Herrington, T. C., Fletcher, C. G., & Kropp, H. (2022). Validation of Pan-Arctic Soil
 1202 Temperatures in Modern Reanalysis and Data Assimilation Systems. *The Cryosphere*
 1203 *Discussions*, 1–33. <https://doi.org/10.5194/tc-2022-5>
 1204 Höglström, E., Heim, B., Bartsch, A., Bergstedt, H., & Pointner, G. (2018). Evaluation of a MetOp
 1205 ASCAT-Derived Surface Soil Moisture Product in Tundra Environments. *Journal of*
 1206 *Geophysical Research: Earth Surface*, 123(12), 3190–3205.
 1207 <https://doi.org/10.1029/2018JF004658>
 1208 Houborg, R., Soegaard, H., & Boegh, E. (2007). Combining vegetation index and model
 1209 inversion methods for the extraction of key vegetation biophysical parameters using
 1210 Terra and Aqua MODIS reflectance data. *Remote Sensing of Environment*, 106(1), 39–
 1211 58. <https://doi.org/10.1016/j.rse.2006.07.016>
 1212 Hugelius, G., Loisel, J., Chadburn, S., Jackson, R. B., Jones, M., MacDonald, G., Marushchak,
 1213 M., Olefeldt, D., Packalen, M., Siewert, M. B., Treat, C., Turetsky, M., Voigt, C., & Yu, Z.
 1214 (2020). Large stocks of peatland carbon and nitrogen are vulnerable to permafrost thaw.
 1215 *Proceedings of the National Academy of Sciences*, 117(34), 20438–20446.
 1216 <https://doi.org/10.1073/pnas.1916387117>
 1217 IPCC AR6. (2023). *AR6 Synthesis Report: Climate Change 2023 — IPCC*.
 1218 <https://www.ipcc.ch/report/sixth-assessment-report-cycle/>
 1219 Irvin, J., Zhou, S., McNicol, G., Lu, F., Liu, V., Fluet-Chouinard, E., Ouyang, Z., Knox, S. H.,
 1220 Lucas-Moffat, A., Trotta, C., Papale, D., Vitale, D., Mammarella, I., Alekseychik, P.,
 1221 Aurela, M., Avati, A., Baldocchi, D., Bansal, S., Bohrer, G., ... Jackson, R. B. (2021).
 1222 Gap-filling eddy covariance methane fluxes: Comparison of machine learning model
 1223 predictions and uncertainties at FLUXNET-CH4 wetlands. *Agricultural and Forest*
 1224 *Meteorology*, 308–309, 108528. <https://doi.org/10.1016/j.agrformet.2021.108528>
 1225 Iwata, H., Harazono, Y., Ueyama, M., Sakabe, A., Nagano, H., Kosugi, Y., Takahashi, K., &
 1226 Kim, Y. (2015). Methane exchange in a poorly-drained black spruce forest over
 1227 permafrost observed using the eddy covariance technique. *Agricultural and Forest*
 1228 *Meteorology*, 214–215, 157–168. <https://doi.org/10.1016/j.agrformet.2015.08.252>

1229 Jiao, M., Zhao, L., Wang, C., Hu, G., Li, Y., Zhao, J., Zou, D., Xing, Z., Qiao, Y., Liu, G., Du, E.,
1230 Xiao, M., & Hou, Y. (2023). Spatiotemporal Variations of Soil Temperature at 10 and 50
1231 cm Depths in Permafrost Regions along the Qinghai-Tibet Engineering Corridor. *Remote*
1232 *Sensing*, 15(2), Article 2. <https://doi.org/10.3390/rs15020455>

1233 Johnson, M. S., Matthews, E., Bastviken, D., Deemer, B., Du, J., & Genovese, V. (2021).
1234 Spatiotemporal Methane Emission From Global Reservoirs. *Journal of Geophysical*
1235 *Research: Biogeosciences*, 126(8), e2021JG006305.
1236 <https://doi.org/10.1029/2021JG006305>

1237 Johnson, M. S., Matthews, E., Du, J., Genovese, V., & Bastviken, D. (2022). Methane Emission
1238 From Global Lakes: New Spatiotemporal Data and Observation-Driven Modeling of
1239 Methane Dynamics Indicates Lower Emissions. *Journal of Geophysical Research:*
1240 *Biogeosciences*, 127(7), e2022JG006793. <https://doi.org/10.1029/2022JG006793>

1241 Jung, M., Reichstein, M., Margolis, H. A., Cescatti, A., Richardson, A. D., Arain, M. A., Arneth,
1242 A., Bernhofer, C., Bonal, D., Chen, J., Gianelle, D., Gobron, N., Kiely, G., Kutsch, W.,
1243 Lasslop, G., Law, B. E., Lindroth, A., Merbold, L., Montagnani, L., ... Williams, C. (2011).
1244 Global patterns of land-atmosphere fluxes of carbon dioxide, latent heat, and sensible
1245 heat derived from eddy covariance, satellite, and meteorological observations. *Journal of*
1246 *Geophysical Research: Biogeosciences*, 116(G3).
1247 <https://doi.org/10.1029/2010JG001566>

1248 Jung, M., Schwalm, C., Migliavacca, M., Walther, S., Camps-Valls, G., Koirala, S., Anthoni, P.,
1249 Besnard, S., Bodesheim, P., Carvalhais, N., Chevallier, F., Gans, F., Goll, D. S., Haverd,
1250 V., Köhler, P., Ichii, K., Jain, A. K., Liu, J., Lombardozzi, D., ... Reichstein, M. (2020).
1251 Scaling carbon fluxes from eddy covariance sites to globe: Synthesis and evaluation of
1252 the FLUXCOM approach. *Biogeosciences*, 17(5), 1343–1365. [https://doi.org/10.5194/bg-](https://doi.org/10.5194/bg-17-1343-2020)
1253 [17-1343-2020](https://doi.org/10.5194/bg-17-1343-2020)

1254 Kim, Y., Johnson, M. S., Knox, S. H., Black, T. A., Dalmagro, H. J., Kang, M., Kim, J., &
1255 Baldocchi, D. (2020). Gap-filling approaches for eddy covariance methane fluxes: A
1256 comparison of three machine learning algorithms and a traditional method with principal
1257 component analysis. *Global Change Biology*, 26(3), 1499–1518.
1258 <https://doi.org/10.1111/gcb.14845>

1259 Kirschke, S., Bousquet, P., Ciais, P., Saunois, M., Canadell, J. G., Dlugokencky, E. J.,
1260 Bergamaschi, P., Bergmann, D., Blake, D. R., Bruhwiler, L., Cameron-Smith, P.,
1261 Castaldi, S., Chevallier, F., Feng, L., Fraser, A., Heimann, M., Hodson, E. L., Houweling,
1262 S., Josse, B., ... Zeng, G. (2013). Three decades of global methane sources and sinks.
1263 *Nature Geoscience*, 6(10), Article 10. <https://doi.org/10.1038/ngeo1955>

1264 Knox, S. H., Bansal, S., McNicol, G., Schafer, K., Sturtevant, C., Ueyama, M., Valach, A. C.,
1265 Baldocchi, D., Delwiche, K., Desai, A. R., Euskirchen, E., Liu, J., Lohila, A., Malhotra, A.,
1266 Melling, L., Riley, W., Runkle, B. R. K., Turner, J., Vargas, R., ... Jackson, R. B. (2021).
1267 Identifying dominant environmental predictors of freshwater wetland methane fluxes
1268 across diurnal to seasonal time scales. *Global Change Biology*, 27(15), 3582–3604.
1269 <https://doi.org/10.1111/gcb.15661>

1270 Knox, S. H., Jackson, R. B., Poulter, B., McNicol, G., Fluet-Chouinard, E., Zhang, Z., Hugelius,
1271 G., Bousquet, P., Canadell, J. G., Saunois, M., Papale, D., Chu, H., Keenan, T. F.,
1272 Baldocchi, D., Torn, M. S., Mammarella, I., Trotta, C., Aurela, M., Bohrer, G., ... Zona, D.

(2019). FLUXNET-CH₄ Synthesis Activity: Objectives, Observations, and Future Directions. *Bulletin of the American Meteorological Society*, 100(12), 2607–2632. <https://doi.org/10.1175/BAMS-D-18-0268.1>

Kuhn, M. A., Varner, R. K., Bastviken, D., Crill, P., MacIntyre, S., Turetsky, M., Walter Anthony, K., McGuire, A. D., & Olefeldt, D. (2021). BAWLD-CH₄: A comprehensive dataset of methane fluxes from boreal and arctic ecosystems. *Earth System Science Data*, 13(11), 5151–5189. <https://doi.org/10.5194/essd-13-5151-2021>

Kuter, S. (2021). Completing the machine learning saga in fractional snow cover estimation from MODIS Terra reflectance data: Random forests versus support vector regression. *Remote Sensing of Environment*, 255, 112294. <https://doi.org/10.1016/j.rse.2021.112294>

Kyzivat, E. D., Smith, L. C., Garcia-Tigreros, F., Huang, C., Wang, C., Langhorst, T., Fayne, J. V., Harlan, M. E., Ishitsuka, Y., Feng, D., Dolan, W., Pitcher, L. H., Wickland, K. P., Dornblaser, M. M., Striegl, R. G., Pavelsky, T. M., Butman, D. E., & Gleason, C. J. (2022). The Importance of Lake Emergent Aquatic Vegetation for Estimating Arctic-Boreal Methane Emissions. *Journal of Geophysical Research: Biogeosciences*, 127(6), e2021JG006635. <https://doi.org/10.1029/2021JG006635>

Larmola, T., Tuittila, E.-S., Tirola, M., Nykänen, H., Martikainen, P. J., Yrjälä, K., Tuomivirta, T., & Fritze, H. (2010). The role of Sphagnum mosses in the methane cycling of a boreal mire. *Ecology*, 91(8), 2356–2365. <https://doi.org/10.1890/09-1343.1>

Lehner, B., & Döll, P. (2004). Development and validation of a global database of lakes, reservoirs and wetlands. *Journal of Hydrology*, 296(1), 1–22. <https://doi.org/10.1016/j.jhydrol.2004.03.028>

Li, M., Wu, P., & Ma, Z. (2020). A comprehensive evaluation of soil moisture and soil temperature from third-generation atmospheric and land reanalysis data sets. *International Journal of Climatology*, 40(13), 5744–5766. <https://doi.org/10.1002/joc.6549>

Li, T., Raivonen, M., Alekseychik, P., Aurela, M., Lohila, A., Zheng, X., Zhang, Q., Wang, G., Mammarella, I., Rinne, J., Yu, L., Xie, B., Vesala, T., & Zhang, W. (2016). Importance of vegetation classes in modeling CH₄ emissions from boreal and subarctic wetlands in Finland. *Science of The Total Environment*, 572, 1111–1122. <https://doi.org/10.1016/j.scitotenv.2016.08.020>

Liebner, S., Zeyer, J., Wagner, D., Schubert, C., Pfeiffer, E.-M., & Knoblauch, C. (2011). Methane oxidation associated with submerged brown mosses reduces methane emissions from Siberian polygonal tundra. *Journal of Ecology*, 99(4), 914–922. <https://doi.org/10.1111/j.1365-2745.2011.01823.x>

Liu, L., Xu, S., Tang, J., Guan, K., Griffis, T. J., Erickson, M. D., Frie, A. L., Jia, X., Kim, T., Miller, L. T., Peng, B., Wu, S., Yang, Y., Zhou, W., Kumar, V., & Jin, Z. (2022). KGML-ag: A modeling framework of knowledge-guided machine learning to simulate agroecosystems: a case study of estimating N₂O emission using data from mesocosm experiments. *Geoscientific Model Development*, 15(7), 2839–2858. <https://doi.org/10.5194/gmd-15-2839-2022>

Ludwig, S. M., Natali, S. M., Schade, J. D., Powell, M., Fiske, G., Schiferl, L. D., & Commane, R. (2023). Scaling waterbody carbon dioxide and methane fluxes in the arctic using an

integrated terrestrial-aquatic approach. *Environmental Research Letters*, 18(6), 064019.
<https://doi.org/10.1088/1748-9326/acd467>

Ma, H., Zeng, J., Zhang, X., Fu, P., Zheng, D., Wigneron, J.-P., Chen, N., & Niyogi, D. (2021). Evaluation of six satellite- and model-based surface soil temperature datasets using global ground-based observations. *Remote Sensing of Environment*, 264, 112605.
<https://doi.org/10.1016/j.rse.2021.112605>

Masson-Delmotte, V., Zhai, P., Pirani, A., Connors, S. L., Péan, C., Berger, S., Caud, N., Chen, Y., Goldfarb, L., & Gomis, M. I. (2021). Climate change 2021: The physical science basis. *Contribution of Working Group I to the Sixth Assessment Report of the Intergovernmental Panel on Climate Change*, 2.

Mastepanov, M., Sigsgaard, C., Dlugokencky, E. J., Houweling, S., Ström, L., Tamstorf, M. P., & Christensen, T. R. (2008). Large tundra methane burst during onset of freezing. *Nature*, 456(7222), Article 7222. <https://doi.org/10.1038/nature07464>

Mavrovic, A., Sonnentag, O., Lemmetyinen, J., Voigt, C., Aurela, M., & Roy, A. (2024). *Winter methane fluxes over boreal and Arctic environments*. ESS Open Archive.
<https://doi.org/10.22541/essoar.170542245.58670859/v1>

McGuire, A. D., Anderson, L. G., Christensen, T. R., Dallimore, S., Guo, L., Hayes, D. J., Heimann, M., Lorensen, T. D., Macdonald, R. W., & Roulet, N. (2009). Sensitivity of the carbon cycle in the Arctic to climate change. *Ecological Monographs*, 79(4), 523–555.
<https://doi.org/10.1890/08-2025.1>

McNicol, G., Fluet-Chouinard, E., Ouyang, Z., Knox, S., Zhang, Z., Aalto, T., Bansal, S., Chang, K.-Y., Chen, M., Delwiche, K., Feron, S., Goeckede, M., Liu, J., Malhotra, A., Melton, J. R., Riley, W., Vargas, R., Yuan, K., Ying, Q., ... Jackson, R. B. (2023). Upscaling Wetland Methane Emissions From the FLUXNET-CH4 Eddy Covariance Network (UpCH4 v1.0): Model Development, Network Assessment, and Budget Comparison. *AGU Advances*, 4(5), e2023AV000956. <https://doi.org/10.1029/2023AV000956>

Melack, J. M., & Hess, L. L. (2023). Areal extent of vegetative cover: A challenge to regional upscaling of methane emissions. *Aquatic Botany*, 184, 103592.
<https://doi.org/10.1016/j.aquabot.2022.103592>

Melton, J. R., Wania, R., Hodson, E. L., Poulter, B., Ringeval, B., Spahni, R., Bohn, T., Avis, C. A., Beerling, D. J., Chen, G., Eliseev, A. V., Denisov, S. N., Hopcroft, P. O., Lettenmaier, D. P., Riley, W. J., Singarayer, J. S., Subin, Z. M., Tian, H., Zürcher, S., ... Kaplan, J. O. (2013). Present state of global wetland extent and wetland methane modelling: Conclusions from a model inter-comparison project (WETCHIMP). *Biogeosciences*, 10(2), 753–788. <https://doi.org/10.5194/bg-10-753-2013>

Miller, S. M., Miller, C. E., Commancie, R., Chang, R. Y.-W., Dinardo, S. J., Henderson, J. M., Karion, A., Lindaas, J., Melton, J. R., Miller, J. B., Sweeney, C., Wofsy, S. C., & Michalak, A. M. (2016). A multiyear estimate of methane fluxes in Alaska from CARVE atmospheric observations. *Global Biogeochemical Cycles*, 30(10), 1441–1453.
<https://doi.org/10.1002/2016GB005419>

Miner, K. R., Turetsky, M. R., Malina, E., Bartsch, A., Tamminen, J., McGuire, A. D., Fix, A., Sweeney, C., Elder, C. D., & Miller, C. E. (2022). Permafrost carbon emissions in a changing Arctic. *Nature Reviews Earth & Environment*, 3(1), Article 1.
<https://doi.org/10.1038/s43017-021-00230-3>

1360 Murray-Hudson, M., Wolski, P., Cassidy, L., Brown, M. T., Thito, K., Kashe, K., & Mosimanyana,
1361 E. (2015). Remote Sensing-derived hydroperiod as a predictor of floodplain vegetation
1362 composition. *Wetlands Ecology and Management*, 23(4), 603–616.
1363 <https://doi.org/10.1007/s11273-014-9340-z>

1364 Natali, S. M., Watts, J. D., Rogers, B. M., Potter, S., Ludwig, S. M., Selbmann, A.-K., Sullivan,
1365 P. F., Abbott, B. W., Arndt, K. A., Birch, L., Björkman, M. P., Bloom, A. A., Celis, G.,
1366 Christensen, T. R., Christiansen, C. T., Commene, R., Cooper, E. J., Crill, P., Czimczik,
1367 C., ... Zona, D. (2019). Large loss of CO₂ in winter observed across the northern
1368 permafrost region. *Nature Climate Change*, 9(11), Article 11.
1369 <https://doi.org/10.1038/s41558-019-0592-8>

1370 Olefeldt, D., Euskirchen, E. S., Harden, J., Kane, E., McGuire, A. D., Waldrop, M. P., &
1371 Turetsky, M. R. (2017). A decade of boreal rich fen greenhouse gas fluxes in response
1372 to natural and experimental water table variability. *Global Change Biology*, 23(6), 2428–
1373 2440. <https://doi.org/10.1111/gcb.13612>

1374 Olefeldt, D., Hovemyr, M., Kuhn, M. A., Bastviken, D., Bohn, T. J., Connolly, J., Crill, P.,
1375 Euskirchen, E. S., Finkelstein, S. A., Genet, H., Grosse, G., Harris, L. I., Heffernan, L.,
1376 Helbig, M., Hugelius, G., Hutchins, R., Juutinen, S., Lara, M. J., Malhotra, A., ... Watts,
1377 J. D. (2021). The Boreal–Arctic Wetland and Lake Dataset (BAWLD). *Earth System
1378 Science Data*, 13(11), 5127–5149. <https://doi.org/10.5194/essd-13-5127-2021>

1379 Olefeldt, D., Turetsky, M. R., Crill, P. M., & McGuire, A. D. (2013). Environmental and physical
1380 controls on northern terrestrial methane emissions across permafrost zones. *Global
1381 Change Biology*, 19(2), 589–603. <https://doi.org/10.1111/gcb.12071>

1382 Osterkamp, T. E., Viereck, L., Shur, Y., Jorgenson, M. T., Racine, C., Doyle, A., & Boone, R. D.
1383 (2000). Observations of Thermokarst and Its Impact on Boreal Forests in Alaska, U.S.A.
1384 *Arctic, Antarctic, and Alpine Research*, 32(3), 303–315.
1385 <https://doi.org/10.1080/15230430.2000.12003368>

1386 Ouyang, Z., Jackson, R. B., McNicol, G., Fluet-Chouinard, E., Runkle, B. R. K., Papale, D.,
1387 Knox, S. H., Cooley, S., Delwiche, K. B., Feron, S., Irvin, J. A., Malhotra, A., Muddasir,
1388 M., Sabbatini, S., Alberto, Ma. C. R., Cescatti, A., Chen, C.-L., Dong, J., Fong, B. N., ...
1389 Zhang, Y. (2023). Paddy rice methane emissions across Monsoon Asia. *Remote
1390 Sensing of Environment*, 284, 113335. <https://doi.org/10.1016/j.rse.2022.113335>

1391 Pallandt, M. M. T. A., Kumar, J., Mauritz, M., Schuur, E. A. G., Virkkala, A.-M., Celis, G.,
1392 Hoffman, F. M., & Göckede, M. (2022). Representativeness assessment of the pan-
1393 Arctic eddy covariance site network and optimized future enhancements.
1394 *Biogeosciences*, 19(3), 559–583. <https://doi.org/10.5194/bg-19-559-2022>

1395 Pedregosa, F., Varoquaux, G., Gramfort, A., Michel, V., Thirion, B., Grisel, O., Blondel, M.,
1396 Prettenhofer, P., Weiss, R., & Dubourg, V. (2011). Scikit-learn: Machine learning in
1397 Python. *The Journal of Machine Learning Research*, 12, 2825–2830.

1398 Peltola, O., Vesala, T., Gao, Y., Rätty, O., Alekseychik, P., Aurela, M., Chojnicki, B., Desai, A.
1399 R., Dolman, A. J., Euskirchen, E. S., Friborg, T., Göckede, M., Helbig, M., Humphreys,
1400 E., Jackson, R. B., Jocher, G., Joos, F., Klatt, J., Knox, S. H., ... Aalto, T. (2019).
1401 Monthly gridded data product of northern wetland methane emissions based on
1402 upscaling eddy covariance observations. *Earth System Science Data*, 11(3), 1263–1289.
1403 <https://doi.org/10.5194/essd-11-1263-2019>

1404 Peng, J., Loew, A., Merlin, O., & Verhoest, N. E. C. (2017). A review of spatial downscaling of
 1405 satellite remotely sensed soil moisture. *Reviews of Geophysics*, 55(2), 341–366.
 1406 <https://doi.org/10.1002/2016RG000543>
 1407 Peng, S., Lin, X., Thompson, R. L., Xi, Y., Liu, G., Hauglustaine, D., Lan, X., Poulter, B.,
 1408 Ramonet, M., Saunois, M., Yin, Y., Zhang, Z., Zheng, B., & Ciais, P. (2022). Wetland
 1409 emission and atmospheric sink changes explain methane growth in 2020. *Nature*,
 1410 612(7940), Article 7940. <https://doi.org/10.1038/s41586-022-05447-w>
 1411 Prigent, C., Jimenez, C., & Bousquet, P. (2020). Satellite-Derived Global Surface Water Extent
 1412 and Dynamics Over the Last 25 Years (GIEMS-2). *Journal of Geophysical Research:*
 1413 *Atmospheres*, 125(3), e2019JD030711. <https://doi.org/10.1029/2019JD030711>
 1414 Rawlins, M. A., Steele, M., Holland, M. M., Adam, J. C., Cherry, J. E., Francis, J. A., Groisman,
 1415 P. Y., Hinzman, L. D., Huntington, T. G., Kane, D. L., Kimball, J. S., Kwok, R., Lammers,
 1416 R. B., Lee, C. M., Lettenmaier, D. P., McDonald, K. C., Podest, E., Pundsack, J. W.,
 1417 Rudels, B., ... Zhang, T. (2010). Analysis of the Arctic System for Freshwater Cycle
 1418 Intensification: Observations and Expectations. *Journal of Climate*, 23(21), 5715–5737.
 1419 <https://doi.org/10.1175/2010JCLI3421.1>
 1420 Reichle, R. H., Lannoy, G. J. M. D., Liu, Q., Koster, R. D., Kimball, J. S., Crow, W. T.,
 1421 Ardizzone, J. V., Chakraborty, P., Collins, D. W., Conaty, A. L., Girotto, M., Jones, L. A.,
 1422 Kolassa, J., Lievens, H., Lucchesi, R. A., & Smith, E. B. (2017). Global Assessment of
 1423 the SMAP Level-4 Surface and Root-Zone Soil Moisture Product Using Assimilation
 1424 Diagnostics. *Journal of Hydrometeorology*, 18(12), 3217–3237.
 1425 <https://doi.org/10.1175/JHM-D-17-0130.1>
 1426 Reichstein, M., Camps-Valls, G., Stevens, B., Jung, M., Denzler, J., Carvalhais, N., & Prabhat.
 1427 (2019). Deep learning and process understanding for data-driven Earth system science.
 1428 *Nature*, 566(7743), Article 7743. <https://doi.org/10.1038/s41586-019-0912-1>
 1429 Rocher-Ros, G., Stanley, E. H., Loken, L. C., Casson, N. J., Raymond, P. A., Liu, S., Amatulli,
 1430 G., & Sponseller, R. A. (2023). Global methane emissions from rivers and streams.
 1431 *Nature*, 621(7979), Article 7979. <https://doi.org/10.1038/s41586-023-06344-6>
 1432 Rosentreter, J. A., Borges, A. V., Deemer, B. R., Holgerson, M. A., Liu, S., Song, C., Melack, J.,
 1433 Raymond, P. A., Duarte, C. M., Allen, G. H., Olefeldt, D., Poulter, B., Battin, T. I., & Eyre,
 1434 B. D. (2021). Half of global methane emissions come from highly variable aquatic
 1435 ecosystem sources. *Nature Geoscience*, 14(4), Article 4. [https://doi.org/10.1038/s41561-](https://doi.org/10.1038/s41561-021-00715-2)
 1436 021-00715-2
 1437 Rößger, N., Sachs, T., Wille, C., Boike, J., & Kutzbach, L. (2022). Seasonal increase of
 1438 methane emissions linked to warming in Siberian tundra. *Nature Climate Change*, 1–6.
 1439 <https://doi.org/10.1038/s41558-022-01512-4>
 1440 Saikia, P., Baruah, R. D., Singh, S. K., & Chaudhuri, P. K. (2020). Artificial Neural Networks in
 1441 the domain of reservoir characterization: A review from shallow to deep models.
 1442 *Computers & Geosciences*, 135, 104357. <https://doi.org/10.1016/j.cageo.2019.104357>
 1443 Saunois, M., Stavert, A. R., Poulter, B., Bousquet, P., Canadell, J. G., Jackson, R. B.,
 1444 Raymond, P. A., Dlugokencky, E. J., Houweling, S., Patra, P. K., Ciais, P., Arora, V. K.,
 1445 Bastviken, D., Bergamaschi, P., Blake, D. R., Brailsford, G., Bruhwiler, L., Carlson, K.
 1446 M., Carol, M., ... Zhuang, Q. (2020). The Global Methane Budget 2000–2017. *Earth*
 1447 *System Science Data*, 12(3), 1561–1623. <https://doi.org/10.5194/essd-12-1561-2020>

1448 Schaaf, C. B., Gao, F., Strahler, A. H., Lucht, W., Li, X., Tsang, T., Strugnell, N. C., Zhang, X.,
 1449 Jin, Y., Muller, J.-P., Lewis, P., Barnsley, M., Hobson, P., Disney, M., Roberts, G.,
 1450 Dunderdale, M., Doll, C., d'Entremont, R. P., Hu, B., ... Roy, D. (2002). First operational
 1451 BRDF, albedo nadir reflectance products from MODIS. *Remote Sensing of Environment*,
 1452 83(1), 135–148. [https://doi.org/10.1016/S0034-4257\(02\)00091-3](https://doi.org/10.1016/S0034-4257(02)00091-3)
 1453 Schiferl, L. D., Watts, J. D., Larson, E. J. L., Arndt, K. A., Biraud, S. C., Euskirchen, E. S.,
 1454 Goodrich, J. P., Henderson, J. M., Kalhori, A., McKain, K., Mountain, M. E., Munger, J.
 1455 W., Oechel, W. C., Sweeney, C., Yi, Y., Zona, D., & Commane, R. (2022). Using
 1456 atmospheric observations to quantify annual biogenic carbon dioxide fluxes on the
 1457 Alaska North Slope. *Biogeosciences*, 19(24), 5953–5972. [https://doi.org/10.5194/bg-19-](https://doi.org/10.5194/bg-19-5953-2022)
 1458 5953-2022
 1459 Smith, S. L., O'Neill, H. B., Isaksen, K., Noetzi, J., & Romanovsky, V. E. (2022). The changing
 1460 thermal state of permafrost. *Nature Reviews Earth & Environment*, 3(1), Article 1.
 1461 <https://doi.org/10.1038/s43017-021-00240-1>
 1462 Spahni, R., Wania, R., Neef, L., van Weele, M., Pison, I., Bousquet, P., Frankenberg, C., Foster,
 1463 P. N., Joos, F., Prentice, I. C., & van Velthoven, P. (2011). Constraining global methane
 1464 emissions and uptake by ecosystems. *Biogeosciences*, 8(6), 1643–1665.
 1465 <https://doi.org/10.5194/bg-8-1643-2011>
 1466 Tramontana, G., Jung, M., Schwalm, C. R., Ichii, K., Camps-Valls, G., Ráduly, B., Reichstein,
 1467 M., Arain, M. A., Cescatti, A., Kiely, G., Merbold, L., Serrano-Ortiz, P., Sickert, S., Wolf,
 1468 S., & Papale, D. (2016). Predicting carbon dioxide and energy fluxes across global
 1469 FLUXNET sites with regression algorithms. *Biogeosciences*, 13(14), 4291–4313.
 1470 <https://doi.org/10.5194/bg-13-4291-2016>
 1471 Treat, C. C., Bloom, A. A., & Marushchak, M. E. (2018). Nongrowing season methane
 1472 emissions—a significant component of annual emissions across northern ecosystems.
 1473 *Global Change Biology*, 24(8), 3331–3343. <https://doi.org/10.1111/gcb.14137>
 1474 Turner, J., Desai, A. R., Thom, J., & Wickland, K. P. (2021). Lagged Wetland CH₄ Flux
 1475 Response in a Historically Wet Year. *Journal of Geophysical Research: Biogeosciences*,
 1476 126(11), e2021JG006458. <https://doi.org/10.1029/2021JG006458>
 1477 Ueyama, M., Iwata, H., Endo, R., & Harazono, Y. (2023). Methane and carbon dioxide
 1478 emissions from the forest floor of a black spruce forest on permafrost in interior Alaska.
 1479 *Polar Science*, 35, 100921. <https://doi.org/10.1016/j.polar.2022.100921>
 1480 Ueyama, M., Knox, S. H., Delwiche, K. B., Bansal, S., Riley, W. J., Baldocchi, D., Hirano, T.,
 1481 McNicol, G., Schafer, K., Windham-Myers, L., Poulter, B., Jackson, R. B., Chang, K.-Y.,
 1482 Chen, J., Chu, H., Desai, A. R., Gogo, S., Iwata, H., Kang, M., ... Sachs, T. (2023).
 1483 Modeled production, oxidation, and transport processes of wetland methane emissions
 1484 in temperate, boreal, and Arctic regions. *Global Change Biology*, 29(8), 2313–2334.
 1485 <https://doi.org/10.1111/gcb.16594>
 1486 Upton, S., Reichstein, M., Gans, F., Peters, W., Kraft, B., & Bastos, A. (2023). Constraining
 1487 biospheric carbon dioxide fluxes by combined top-down and bottom-up approaches.
 1488 *EGU sphere*, 1–31. <https://doi.org/10.5194/egusphere-2023-805>
 1489 van Hulzen, J. B., Segers, R., van Bodegom, P. M., & Leffelaar, P. A. (1999). Temperature
 1490 effects on soil methane production: An explanation for observed variability. *Soil Biology*
 1491 *and Biochemistry*, 31(14), 1919–1929. [https://doi.org/10.1016/S0038-0717\(99\)00109-1](https://doi.org/10.1016/S0038-0717(99)00109-1)

1492 Villarreal, S., & Vargas, R. (2021). Representativeness of FLUXNET Sites Across Latin
1493 America. *Journal of Geophysical Research: Biogeosciences*, 126(3), e2020JG006090.
1494 <https://doi.org/10.1029/2020JG006090>

1495 Virkkala, A.-M., Aalto, J., Rogers, B. M., Tagesson, T., Treat, C. C., Natali, S. M., Watts, J. D.,
1496 Potter, S., Lehtonen, A., Mauritz, M., Schuur, E. A. G., Kochendorfer, J., Zona, D.,
1497 Oechel, W., Kobayashi, H., Humphreys, E., Goeckede, M., Iwata, H., Lafleur, P. M., ...
1498 Luoto, M. (2021). Statistical upscaling of ecosystem CO₂ fluxes across the terrestrial
1499 tundra and boreal domain: Regional patterns and uncertainties. *Global Change Biology*,
1500 27(17), 4040–4059. <https://doi.org/10.1111/gcb.15659>

1501 Virkkala, A.-M., Niittynen, P., Kemppinen, J., Marushchak, M. E., Voigt, C., Hensgens, G.,
1502 Kerttula, J., Happonen, K., Tyystjärvi, V., Biasi, C., Hultman, J., Rinne, J., & Luoto, M.
1503 (2023). High-resolution spatial patterns and drivers of terrestrial ecosystem carbon
1504 dioxide, methane, and nitrous oxide fluxes in the tundra. *Biogeosciences Discussions*,
1505 1–29. <https://doi.org/10.5194/bg-2023-61>

1506 Voigt, C., Virkkala, A.-M., Hould Gosselin, G., Bennett, K. A., Black, T. A., Detto, M., Chevrier-
1507 Dion, C., Guggenberger, G., Hashmi, W., Kohl, L., Kou, D., Marquis, C., Marsh, P.,
1508 Marushchak, M. E., Nesic, Z., Nykänen, H., Saarela, T., Sauheitl, L., Walker, B., ...
1509 Sonnentag, O. (2023). Arctic soil methane sink increases with drier conditions and
1510 higher ecosystem respiration. *Nature Climate Change*, 13(10), Article 10.
1511 <https://doi.org/10.1038/s41558-023-01785-3>

1512 Walsh, J. E. (2014). Intensified warming of the Arctic: Causes and impacts on middle latitudes.
1513 *Global and Planetary Change*, 117, 52–63.
1514 <https://doi.org/10.1016/j.gloplacha.2014.03.003>

1515 Wang, W., Rinke, A., Moore, J. C., Ji, D., Cui, X., Peng, S., Lawrence, D. M., McGuire, A. D.,
1516 Burke, E. J., Chen, X., Decharme, B., Koven, C., MacDougall, A., Saito, K., Zhang, W.,
1517 Alkama, R., Bohn, T. J., Ciais, P., Delire, C., ... Sherstiukov, A. B. (2016). Evaluation of
1518 air–soil temperature relationships simulated by land surface models during winter across
1519 the permafrost region. *The Cryosphere*, 10(4), 1721–1737. <https://doi.org/10.5194/tc-10-1721-2016>

1521 Wang, Z., Schaaf, C. B., Sun, Q., Shuai, Y., & Román, M. O. (2018). Capturing rapid land
1522 surface dynamics with Collection V006 MODIS BRDF/NBAR/Albedo (MCD43) products.
1523 *Remote Sensing of Environment*, 207, 50–64. <https://doi.org/10.1016/j.rse.2018.02.001>

1524 Watts, J. D., Farina, M., Kimball, J. S., Schiferl, L. D., Liu, Z., Arndt, K. A., Zona, D., Ballantyne,
1525 A., Euskirchen, E. S., Parmentier, F.-J. W., Helbig, M., Sonnentag, O., Tagesson, T.,
1526 Rinne, J., Ikawa, H., Ueyama, M., Kobayashi, H., Sachs, T., Nadeau, D. F., ... Oechel,
1527 W. C. (2023). Carbon uptake in Eurasian boreal forests dominates the high-latitude net
1528 ecosystem carbon budget. *Global Change Biology*, 29(7), 1870–1889.
1529 <https://doi.org/10.1111/gcb.16553>

1530 Watts, J. D., Kimball, J. S., Parmentier, F. J. W., Sachs, T., Rinne, J., Zona, D., Oechel, W.,
1531 Tagesson, T., Jackowicz-Korczyński, M., & Aurela, M. (2014). A satellite data driven
1532 biophysical modeling approach for estimating northern peatland and tundra
1533 CO₂ and CH₄ fluxes. *Biogeosciences*,
1534 11(7), 1961–1980. <https://doi.org/10.5194/bg-11-1961-2014>

Wik, M., Varner, R. K., Anthony, K. W., MacIntyre, S., & Bastviken, D. (2016). Climate-sensitive northern lakes and ponds are critical components of methane release. *Nature Geoscience*, 9(2), Article 2. <https://doi.org/10.1038/ngeo2578>

Wrona, E., Rowlandson, T. L., Nambiar, M., Berg, A. A., Colliander, A., & Marsh, P. (2017). Validation of the Soil Moisture Active Passive (SMAP) satellite soil moisture retrieval in an Arctic tundra environment. *Geophysical Research Letters*, 44(9), 4152–4158. <https://doi.org/10.1002/2017GL072946>

Yamazaki, D., Ikeshima, D., Tawatari, R., Yamaguchi, T., O'Loughlin, F., Neal, J. C., Sampson, C. C., Kanae, S., & Bates, P. D. (2017). A high-accuracy map of global terrain elevations. *Geophysical Research Letters*, 44(11), 5844–5853. <https://doi.org/10.1002/2017GL072874>

Avis, C. A., Weaver, A. J., & Meissner, K. J. (2011). Reduction in areal extent of high-latitude wetlands in response to permafrost thaw. *Nature Geoscience*, 4(7), 444–448. <https://doi.org/10.1038/ngeo1160>

Bansal, S., Creed, I. F., Tangen, B. A., Bridgman, S. D., Desai, A. R., Krauss, K. W., Neubauer, S. C., Noe, G. B., Rosenberry, D. O., Trettin, C., Wickland, K. P., Allen, S. T., Arias-Ortiz, A., Armitage, A. R., Baldocchi, D., Banerjee, K., Bastviken, D., Berg, P., Bogard, M. J., ... Zhu, X. (2023). Practical Guide to Measuring Wetland Carbon Pools and Fluxes. *Wetlands*, 43(8), 105. <https://doi.org/10.1007/s13157-023-01722-2>

Bartsch, A., Efimova, A., Widhalm, B., Muri, X., von Baeckmann, C., Bergstedt, H., Ermokhina, K., Hugelius, G., Heim, B., & Leibman, M. (2024). Circumarctic land cover diversity considering wetness gradients. *Hydrology and Earth System Sciences*, 28(11), 2421–2481. <https://doi.org/10.5194/hess-28-2421-2024>

Baskaran, L., Elder, C., Bloom, A. A., Ma, S., Thompson, D., & Miller, C. E. (2022). Geomorphological patterns of remotely sensed methane hot spots in the Mackenzie Delta, Canada. *Environmental Research Letters*, 17(1), 015009. <https://doi.org/10.1088/1748-9326/ac41fb>

Chu, H., Luo, X., Ouyang, Z., Chan, W. S., Dengel, S., Biraud, S. C., Torn, M. S., Metzger, S., Kumar, J., Arain, M. A., Arkebauer, T. J., Baldocchi, D., Bernacchi, C., Billesbach, D., Black, T. A., Blanken, P. D., Bohrer, G., Bracho, R., Brown, S., ... Zona, D. (2021). Representativeness of Eddy-Covariance flux footprints for areas surrounding AmeriFlux sites. *Agricultural and Forest Meteorology*, 301–302, 108350. <https://doi.org/10.1016/j.agrformet.2021.108350>

Elder, C. D., Thompson, D. R., Thorpe, A. K., Chandanpurkar, H. A., Hanke, P. J., Hasson, N., James, S. R., Minsley, B. J., Pastick, N. J., Olefeldt, D., Walter Anthony, K. M., & Miller, C. E. (2021). Characterizing Methane Emission Hotspots From Thawing Permafrost. *Global Biogeochemical Cycles*, 35(12), e2020GB006922. <https://doi.org/10.1029/2020GB006922>

Gelaro, R., McCarty, W., Suárez, M. J., Todling, R., Molod, A., Takacs, L., Randles, C. A., Darmenov, A., Bosilovich, M. G., Reichle, R., Wargan, K., Coy, L., Cullather, R., Draper, C., Akella, S., Buchard, V., Conaty, A., Silva, A. M. da, Gu, W., ... Zhao, B. (2017). The Modern-Era Retrospective Analysis for Research and Applications, Version 2 (MERRA-2). *Journal of Climate*, 30(14), 5419–5454. <https://doi.org/10.1175/JCLI-D-16-0758.1>

1578 Kuhn, M. A., Varner, R. K., Bastviken, D., Crill, P., MacIntyre, S., Turetsky, M., Walter Anthony,
1579 K., McGuire, A. D., & Olefeldt, D. (2021). BAWLD-CH₄: A comprehensive dataset of
1580 methane fluxes from boreal and arctic ecosystems. *Earth System Science Data*, 13(11),
1581 5151–5189. <https://doi.org/10.5194/essd-13-5151-2021>

1582 Lehner, B., Anand, M., Fluet-Chouinard, E., Tan, F., Aires, F., Allen, G. H., Bousquet, P.,
1583 Canadell, J. G., Davidson, N., Finlayson, C. M., Gumbrecht, T., Hilarides, L., Hugelius,
1584 G., Jackson, R. B., Korver, M. C., McIntyre, P. B., Nagy, S., Olefeldt, D., Pavelsky, T.
1585 M., ... Thieme, M. (2024). Mapping the world's inland surface waters: An update
1586 to the Global Lakes and Wetlands Database (GLWD v2). *Earth System Science Data*
1587 *Discussions*, 1–49. <https://doi.org/10.5194/essd-2024-204>

1588 Mastepanov, M., Sigsgaard, C., Dlugokencky, E. J., Houweling, S., Ström, L., Tamstorf, M. P., &
1589 Christensen, T. R. (2008). Large tundra methane burst during onset of freezing. *Nature*,
1590 456(7222), Article 7222. <https://doi.org/10.1038/nature07464>

1591 Miller, S. M., Miller, C. E., Commance, R., Chang, R. Y.-W., Dinardo, S. J., Henderson, J. M.,
1592 Karion, A., Lindaas, J., Melton, J. R., Miller, J. B., Sweeney, C., Wofsy, S. C., &
1593 Michalak, A. M. (2016). A multiyear estimate of methane fluxes in Alaska from CARVE
1594 atmospheric observations. *Global Biogeochemical Cycles*, 30(10), 1441–1453.
1595 <https://doi.org/10.1002/2016GB005419>

1596 Ramage, J., Kuhn, M., Virkkala, A.-M., Voigt, C., Marushchak, M. E., Bastos, A., Biasi, C.,
1597 Canadell, J. G., Ciais, P., López-Blanco, E., Natali, S. M., Olefeldt, D., Potter, S.,
1598 Poulter, B., Rogers, B. M., Schuur, E. A. G., Treat, C., Turetsky, M. R., Watts, J., &
1599 Hugelius, G. (2024). The Net GHG Balance and Budget of the Permafrost Region
1600 (2000–2020) From Ecosystem Flux Upscaling. *Global Biogeochemical Cycles*, 38(4),
1601 e2023GB007953. <https://doi.org/10.1029/2023GB007953>

1602 Thornton, B. F., Wik, M., & Crill, P. M. (2016). Double-counting challenges the accuracy of high-
1603 latitude methane inventories. *Geophysical Research Letters*, 43(24), 12,569–12,577.
1604 <https://doi.org/10.1002/2016GL071772>

1605 Treat, C. C., Virkkala, A.-M., Burke, E., Bruhwiler, L., Chatterjee, A., Fisher, J. B., Hashemi, J.,
1606 Parmentier, F.-J. W., Rogers, B. M., Westermann, S., Watts, J. D., Blanc-Betes, E.,
1607 Fuchs, M., Kruse, S., Malhotra, A., Miner, K., Strauss, J., Armstrong, A., Epstein, H.
1608 E., ... Hugelius, G. (2024). Permafrost Carbon: Progress on Understanding Stocks and
1609 Fluxes Across Northern Terrestrial Ecosystems. *Journal of Geophysical Research:*
1610 *Biogeosciences*, 129(3), e2023JG007638. <https://doi.org/10.1029/2023JG007638>

1611

1612 Yuan, K., Li, F., McNicol, G., Chen, M., Hoyt, A., Knox, S., Riley, W. J., Jackson, R., & Zhu, Q.
1613 (2024). Boreal–Arctic wetland methane emissions modulated by warming and vegetation
1614 activity. *Nature Climate Change*, 1–7. <https://doi.org/10.1038/s41558-024-01933-3>

1615 Yuan, K., Zhu, Q., Li, F., Riley, W. J., Torn, M., Chu, H., McNicol, G., Chen, M., Knox, S.,
1616 Delwiche, K., Wu, H., Baldocchi, D., Ma, H., Desai, A. R., Chen, J., Sachs, T., Ueyama,
1617 M., Sonnentag, O., Helbig, M., ... Jackson, R. (2022). Causality guided machine learning
1618 model on wetland CH₄ emissions across global wetlands. *Agricultural and Forest*
1619 *Meteorology*, 324, 109115. <https://doi.org/10.1016/j.agrformet.2022.109115>

1620 Zhang, C., Comas, X., & Brodylo, D. (2020). A Remote Sensing Technique to Upscale Methane
1621 Emission Flux in a Subtropical Peatland. *Journal of Geophysical Research:*
1622 *Biogeosciences*, 125(10), e2020JG006002. <https://doi.org/10.1029/2020JG006002>
1623 Zhang, Z., Bansal, S., Chang, K.-Y., Fluët-Chouinard, E., Delwiche, K., Goeckede, M.,
1624 Gustafson, A., Knox, S., Leppänen, A., Liu, L., Liu, J., Malhotra, A., Markkanen, T.,
1625 McNicol, G., Melton, J. R., Miller, P. A., Peng, C., Raivonen, M., Riley, W. J., ... Poulter,
1626 B. (2023). Characterizing Performance of Freshwater Wetland Methane Models Across
1627 Time Scales at FLUXNET-CH4 Sites Using Wavelet Analyses. *Journal of Geophysical*
1628 *Research: Biogeosciences*, 128(11), e2022JG007259.
1629 <https://doi.org/10.1029/2022JG007259>
1630 Zhang, Z., Fluët-Chouinard, E., Jensen, K., McDonald, K., Hugelius, G., Gumbrecht, T., Carroll,
1631 M., Prigent, C., Bartsch, A., & Poulter, B. (2021). Development of the global dataset of
1632 Wetland Area and Dynamics for Methane Modeling (WAD2M). *Earth System Science*
1633 *Data*, 13(5), 2001–2023. <https://doi.org/10.5194/essd-13-2001-2021>
1634 Zhang, Z., Poulter, B., Feldman, A. F., Ying, Q., Ciais, P., Peng, S., & Li, X. (2023). Recent
1635 intensification of wetland methane feedback. *Nature Climate Change*, 13(5), Article 5.
1636 <https://doi.org/10.1038/s41558-023-01629-0>
1637 Zona, D., Gioli, B., Commane, R., Lindaas, J., Wofsy, S. C., Miller, C. E., Dinardo, S. J., Dengel,
1638 S., Sweeney, C., Karion, A., Chang, R. Y.-W., Henderson, J. M., Murphy, P. C.,
1639 Goodrich, J. P., Moreaux, V., Liljedahl, A., Watts, J. D., Kimball, J. S., Lipson, D. A., &
1640 Oechel, W. C. (2016). Cold season emissions dominate the Arctic tundra methane
1641 budget. *Proceedings of the National Academy of Sciences*, 113(1), 40–45.
1642 <https://doi.org/10.1073/pnas.1516017113>